

**PARAMETRICALLY-EXCITED MICROELECTROMECHANICAL
OSCILLATORS WITH FILTERING CAPABILITIES**

By

Jeffrey Frederick Rhoads

A THESIS

Submitted to
Michigan State University
in partial fulfillment of the requirements
for the degree of

MASTER OF SCIENCE

Department of Mechanical Engineering

2004

ABSTRACT

PARAMETRICALLY-EXCITED MICROELECTROMECHANICAL OSCILLATORS WITH FILTERING CAPABILITIES

By

Jeffrey Frederick Rhoads

This thesis investigates a class of tunable microelectromechanical (MEM) oscillators that can be implemented in systems that act as signal filters. Unlike most mechanical and electrical filters that rely on direct linear resonance for filtering, the MEM filters presented in this work employ parametric resonance. As a result, these filters feature, in addition to the general benefits associated with MEM devices, nearly ideal stopband rejection and extremely sharp response roll-off. Unfortunately, the introduction of parametric instabilities into the system does present some complications with regard to filtering. These issues are addressed by means of novel tuning schemes and logic implementation that make use of a pair of MEM oscillators and associated circuitry. This thesis includes a brief introduction to bandpass filters, an analysis of a dynamic model for electrostatically driven MEM oscillators, descriptions of methods by which the aforementioned deficiencies can be overcome by parameter selection and tuning, and a method through which two MEM oscillators can be combined to yield a highly effective MEM bandpass filter.

To my parents, for their continual support.

ACKNOWLEDGEMENTS

This work would not have been possible without the assistance and guidance of my advisor, Dr. Steven Shaw. I would also like to thank Barry Demartini, Dr. Kimberly Turner, and the other members of the MEMS Characterization Laboratory at the University of California, Santa Barbara for the integral role they played in this work, and especially for contributing preliminary design information and MEM oscillator images to this endeavor. Additional thanks go to the Air Force Office of Scientific Research for providing the necessary funding for the project, Drs. Cevat Gokcek and Alan Haddow for providing valuable insight and sitting on my committee, and to my colleague, Brian Olson, for acting as a sounding board throughout this research.

Table of Contents

LIST OF TABLES.....	vi
LIST OF FIGURES.....	vii
CHAPTER 1	
Introduction and Background.....	1
CHAPTER 2	
Bandpass Filter Specifications.....	6
CHAPTER 3	
Employing Parametric Resonance for Filtering.....	10
CHAPTER 4	
THE Dynamics of a Single Parametrically-Excited MEM Oscillator.....	17
CHAPTER 5	
Linear Tuning: Manipulating the Instability Zone.....	28
CHAPTER 6	
Nonlinear Tuning: Conditioning the Nontrivial Response.....	33
6.1 Averaged Equations of Motion.....	33
6.2 Analysis of the Steady-State Responses.....	35
6.3 Tuning the MEM Oscillator's Nonlinearity.....	55
6.4 Summary.....	60
CHAPTER 7	
Creating a Bandpass Filter.....	62
CHAPTER 8	
Design Robustness Issues.....	68
8.1 Parameter Sensitivity.....	69
8.2 Effects of Noise.....	73
CHAPTER 9	
Conclusions and Directions for Future Work.....	75
REFERENCES.....	77

LIST OF TABLES

Table 1. Nondimensional parameter definitions [1, 2].

Table 2. A comprehensive list of the design parameters used throughout this work [1].

Table 3. Redefined nondimensional parameters [1, 2].

Table 4. Summary of tuning requirements for bandpass filtering [1]. The “Nonlinearity Region” refers to Figure 9.

LIST OF FIGURES

Figure 1. A sample frequency response function for a bandpass filter (Adapted from [3]).

Figure 2. An approximate Strutt-Ince stability chart for the linear Mathieu equation ($\mu = 0$) near principle parametric resonance. “U” denotes those regions wherein the equation’s trivial solution is unstable. Likewise, “S” denotes those regions wherein the trivial solution is stable. Note that with the addition of small damping the transition curve emanating from $\Omega = 2$ shifts upward in the parameter space, most notably near the vertex.

Figure 3. The dominant instability zone in the $\Omega - \lambda$ parameter space with a superimposed nonlinear frequency response for a given value of λ (Adapted from [4]); (a) with hardening nonlinearity ($\mu > 0$) (b) with softening nonlinearity ($\mu < 0$). Note that solid lines indicate a stable response and dashed lines indicate an unstable response. Also shown is the effect of damping on the instability region.

Figure 4. Schematic of both interdigitated and non-interdigitated electrostatic comb drives (Adapted from [5]). The arrows designate the dominant direction of motion. (a) An interdigitated comb drive. (b) A non-interdigitated comb drive in an ‘aligned’ position. (c) A non-interdigitated comb drive in a ‘misaligned’ position.

Figure 5. (a) A representative parametrically excited MEM oscillator [1]. (b) A close up view of the non-interdigitated comb drives [1]. The oscillator’s backbone “B” is the primary mass, the springs “S” provide attachment to ground as well as the mechanical restoring force, and the non-interdigitated comb drives “N” are used to provide parametric excitation. “AC” and “DC” indicate voltage sources. [Pictures courtesy of Barry Demartini and Dr. Kimberly Turner, University of California, Santa Barbara.]

Figure 6. A CAD drawing of a representative MEM oscillator [1].

Figure 7. The regions of parametric instability in the $V_A - \Omega$ parameter space produced using both the system’s averaged equations and simulations of the system’s full equation of motion with the linear parameters defined in Table 2. (a) The case of pure AC voltage excitation. (b) A nominal case which results in a symmetric wedge of instability [1].

Figure 8. Parametric instability zones in the $V_A - \Omega$ parameter space (for $r_{1A} > 0$) created using both analytical techniques and simulations. (a) $\rho = 0$ and $\rho = 1/2$. (b) $\rho = 0$ and $\rho = -1/2$.

Figure 9. The $\gamma_3 - \lambda_3$ parameter space [6]. The roman numerals are used to designate the various response regions.

Figure 10. Representative frequency response plots showing response amplitude versus detuning frequency for each of the eight regions delineated in Figure 8 [6]. The frequency regions designated by the letters correspond to the phase portraits of Figure 11.

Figure 11. Representative phase plots corresponding to the frequency response regions defined in Figure 9 [6]. Solid dots indicate equilibrium points.

Figure 12. Sample parameter spaces showing how the oscillator's nonlinearity can transition between response regimes under a varying input excitation amplitude; (a) for the $\rho = -1/2$ design presented in Table 2, (b) for the $\rho = 1/2$ design presented in Table 2 [6].

Figure 13. Sample response curves – amplitude vs. frequency: (a) $\rho = 1/2$ and (b) $\rho = -1/2$.

Figure 14. One proposed logic implementation scheme, which is capable of producing a bandpass filter [1, 2].

Figure 15. Simulation results from the filter system of Figure 14 [1]. Data points are frequency thresholds for the passband boundaries at various AC amplitude levels. The insets show the system outputs at the points indicated.

Figure 16. Sensitivity plots, which show the sensitivity of ρ with respect to each of its components. The black squares designate the nominal design parameters used for the $\rho = 1/2$ oscillator under consideration here.

Chapter 1

Introduction and Background

As the demand for commercial and tactical wireless communications devices continues to increase, so too does the demand for effective and efficient bandpass signal filters. These devices, used to attenuate signals with frequency components outside of a specific bandwidth while passing those within, are an integral part of such technology. This is especially true in the case of cellular phones, the driving force in the wireless communications industry.

Due to its importance in a number of applications, bandpass filter design has been considered a viable research topic since the late 19th century. However, it was not until the early 20th century that the full potential of bandpass filters was realized. At that time engineers working at Bell Laboratories showed the potential of electrical, and later mechanical, bandpass filters in practical engineering applications, such as phonographs [7-10].

Since then, filter research has undergone a steady progression, with numerous design alternatives being proposed. Amongst the mechanical and

electromechanical filter designs brought forth, one specifically stands out, namely the design proposed by Adler in the late 1940s [10, 11]. This design, which utilized weakly-coupled mechanical resonators to produce a narrow banded frequency response function, exhibited high quality factors (defined in the case of bandpass filters as the ratio between the filter's resonant frequency and its bandwidth) and much improved operational stability compared to its predecessors. Following Adler, numerous filter designs appeared that utilized ceramic and quartz crystal resonators [12-14]. While these designs advanced the capabilities of mechanical filters, they tended to be bulky in comparison with other designs and thus were utilized in a limited number of applications.

Despite differing in form and appearance, each of the mechanical and electromechanical filter designs proposed in the early to mid 20th century exhibited a number of common characteristics. Most significantly, each featured a relatively high quality (Q) factor and robust operational stability. However, they proved to be costly and generally incompatible with integrated circuitry and thus had limited potential following the emergence of such technology in the late 20th century.

In the electronic rich era of the late 20th century, filter design focused primarily on electrical and electromechanical bandpass filters (see, for example, [14-18]). The proposed designs consisted of chains of coupled resonators, such as RLC circuits, and also more modern technologies, such as surface acoustic

waves (SAWs) [16-18] and even discrete-time digital systems [14, 19-22]. In comparison to their predecessors, these designs offer ease of integration with IC technology. However, they too exhibit somewhat limited potential in some filtering applications due to limitations in their size, frequency operating ranges, and quality factors [18].

The introduction of microelectromechanical (MEM) devices into mainstream engineering has opened a promising new path of study regarding the development of filters [1-3, 23-28]. This promise is founded upon the distinct advantages MEM filters hold over more conventional designs. Namely, MEM filters are typically smaller, consume less power to operate, and have the potential to operate with significantly higher Q factors. MEM filters also offer seamless integration with IC technology and are highly tunable in nature.

To date, a number of MEM filter designs have been proposed, with the three most prevalent designs being the electrostatically-driven coupled resonator filter, the electrostatically-driven clamped-clamped beam filter, and the piezoelectrically-driven clamped-clamped beam filter. The coupled resonator filter, popularized primarily by Nguyen and Howe [3, 23-25, 29-31], utilizes a design similar to that proposed by Adler nearly sixty years ago, but developed at microscale. This design has gained popularity largely due to the exceedingly high Q factors it produces, which, have been reported to be as high as 80,000 in vacuum [3]. An alternative design proposed Nguyen [25, 29, 32, 33] utilizes an

electrostatically-driven clamped-clamped beam filter. While the Q factors reported for this filter are significantly lower (about 8000), the clamped-clamped beam design is both smaller and easier to fabricate. An analogous design proposed by Piekarski, et al [26] also utilizes a single clamped-clamped beam resonator, but excited through piezoelectric means. While the Q factors reported for this filter are significantly lower than those reported for both the coupled resonator and electrostatically-driven clamped-clamped beam filter designs (about 1000), the piezoelectrically-driven clamped-clamped beam design does not require the specially tailored input (no bias voltage is required) and drive electrodes of its counterparts and is easy to fabricate.

Whereas the three filter designs discussed above utilize coupled oscillators and/or linear phenomena for filtering, the present work describes a filter design based on the nonlinear response of parametrically-excited MEM oscillators. With further development, this design may have significant potential in many communications applications. The thesis is outlined as follows. Chapter 2 reviews some basic information with regards to filter design and performance. Chapter 3 reviews parametric resonance and discusses its relevance to MEMS and its potential use in filtering applications. In Chapter 4, a single MEM oscillator is modeled and its dynamic response is analyzed. Chapters 5 and 6 present tuning schemes, linear and nonlinear, respectively, that are capable of improving oscillator performance, specifically for filtering applications. Chapter 7 describes one possible filter design which utilizes two tuned MEM oscillators.

The robustness of the proposed filter design is examined in Chapter 8, and the thesis concludes in Chapter 9 with a brief discussion and some concluding remarks. Note that a considerable portion of this work has been submitted for publication in three papers that were co-authored by the author [1, 2, 6].

Chapter 2

Bandpass Filter Specifications

The subject of this thesis is bandpass filters, which are systems that pass the components of signals, ideally unaltered, with frequencies inside a specified passband, while attenuating those components outside of the passband. Since Adler's development in the 1940s, most bandpass filter designs have been based on a one-dimensional chain of identical resonators. In such an approach, the natural frequency of the system determines the filter's center frequency (see Figure 1). Weak coupling (generally of the 'nearest neighbor' type) is then used to produce a system with multiple natural frequencies in close proximity to the filter's center frequency. An input signal is provided at one end of the resonator chain and the system response, a filtered version of the input, is measured at the opposite end. The result, when the system is operated in a lightly damped environment (vacuum or partial vacuum in the case of MEMS), is a highly desirable filter frequency response function (FRF), which features closely packed, lightly damped resonances, as shown in Figure 1.

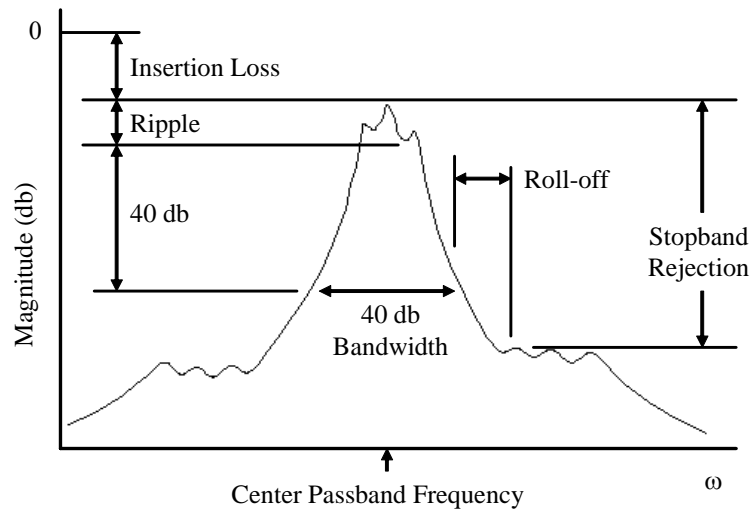


Figure 1. A sample frequency response function for a bandpass filter (Adapted from [3]).

Figure 1 highlights some of the key features which should be considered when designing a bandpass filter or assessing a filter's performance. The characteristics of greatest interest are [1, 2, 14]:

- The center passband frequency – the nominal operating frequency of the filter.
- The bandwidth – the range of frequencies that will pass through the filter with minimal loss in signal strength.
- The stopband rejection – the amount by which the signal is attenuated outside of the passband.
- The insertion loss – the reduction in signal amplitude as the signal passes through the filter.
- The sharpness of the roll-off – the width of the frequency range between the edges of the passband and the stopband.

- The flatness of the passband response – the degree to which ripples are present in the filter’s passband frequency response.

Note that the aforementioned linear filters can be designed to exhibit near-optimal characteristics. In fact, a number of well established design techniques exist whose sole purpose is optimizing the performance of certain filter properties [14, 15, 34], though often to the detriment of others. Chebyshev design, for example, results in a filter with an equiripple passband and monotonic stopband, but only average roll-off characteristics. Similarly, Butterworth filter design generates both a monotonic stopband and a monotonic passband, but at the cost of poor roll-off characteristics. Other design approaches include elliptical design, which yields a highly selective filter with extremely sharp response roll-off, but also distinct ripples in both the passband and stopband, and Bessel design, which produces excellent time response characteristics and a linearly-varying phase, but also poor rejection characteristics. Independent of the design method is the fact that the shape of the respective FRF is altered by increasing the filter’s order or, in filters based on Adler’s design, adding additional oscillators to the chain. Thus, while certain filter characteristics can be optimized, it is usually done at the expense of the filter’s other response characteristics, its complexity, and its insertion loss. In comparison, it is believed that the performance characteristics of the proposed parametrically-excited MEM filter are largely independent of one another and can be optimized individually with

minimal change in overall performance [1, 2]. However, this can be achieved only by exploiting special parameter tuning, which is readily achievable in MEMS.

Chapter 3

Employing Parametric Resonance for Filtering

Parametric excitation is a form of excitation that affects a system's response only when the states of the system are non-zero. Mathematically this means one or more of the coefficients of the dynamic states in a system's equation of motion are time varying. Originally discovered by Faraday in the 1830s during experimentation with a vertically excited column of water [35, 36], parametric excitation is mathematically exemplified today by a special case of the Hill equation, the Mathieu equation, which can be expressed as

$$z'' + (1 + \lambda \cos \Omega \tau)z + \mu z^3 = 0. \quad (3.1)$$

While this equation can be used to describe a variety of electrical and mechanical systems, the most prevalent physical model is that of a single pendulum with purely vertical base excitation. In this system, periodic excitation

at the pendulum's base produces an oscillating effective gravity, which, in turn, leads to the time varying effective stiffness in the system's equation of motion.

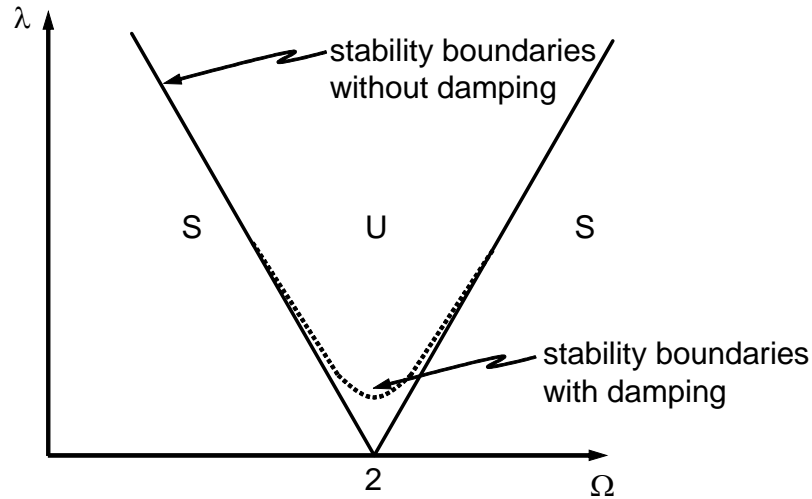


Figure 2. An approximate Strutt-Ince stability chart for the linear Mathieu equation ($\mu = 0$) near principle parametric resonance. “U” denotes those regions wherein the equation’s trivial solution is unstable. Likewise, “S” denotes those regions wherein the trivial solution is stable. Note that with the addition of small damping the transition curve emanating from $\Omega = 2$ shifts upward in the parameter space, most notably near the vertex.

The response characteristics of the Mathieu system are well understood, in particular, the effects of variations in the system’s damping (not included in the model presented above), excitation amplitude, forcing frequency, natural frequency, and nonlinearities (also not shown) are known (see, for example, [35, 37-44]). Of direct relevance to this work are the stability and resonance characteristics of a parametrically-excited system (such as Equation 3.1). To explore this further, first consider the Strutt-Ince stability chart shown in Figure 2,

developed by van der Pol and Strutt in 1928 [38], which delineates the stability of the trivial response of the Mathieu equation (Equation 3.1) in terms of the parameters Ω and λ . Of direct relevance here is that within certain parameter regions, hereafter referred to as “instability zones” or “wedges of instability”, the trivial response becomes unstable and, in fact, unbounded in the absence of nonlinearities. While the addition of damping has no impact with regard to limiting the unstable response, it does produce a fundamental change in the Strutt-Ince stability chart. Namely, it shifts the transition curves, such as those emanating from $\Omega = 2$, upward in the parameter space. Figure 2 shows this for the $\Omega = 2$ case. The addition of nonlinearities in the system can limit the response inside the instability zones. In particular, this addition leads to nontrivial steady-state responses within the unstable domain. These solutions may or may not persist outside of the unstable domains, depending on the types and magnitudes of both the nonlinearity and the damping, but when they do persist, the solutions coexist with the stable trivial solution, which results in hysteresis in the system’s frequency response. Examples of this situation are shown in Figures 3(a) and 3(b) for hardening and softening nonlinearities, respectively. The amplitude dependent nature of the bandwidth of the instability zone should also be noted. In particular, it is observed that as the parametric excitation amplitude, λ , is increased the bandwidth of the instability zone increases.

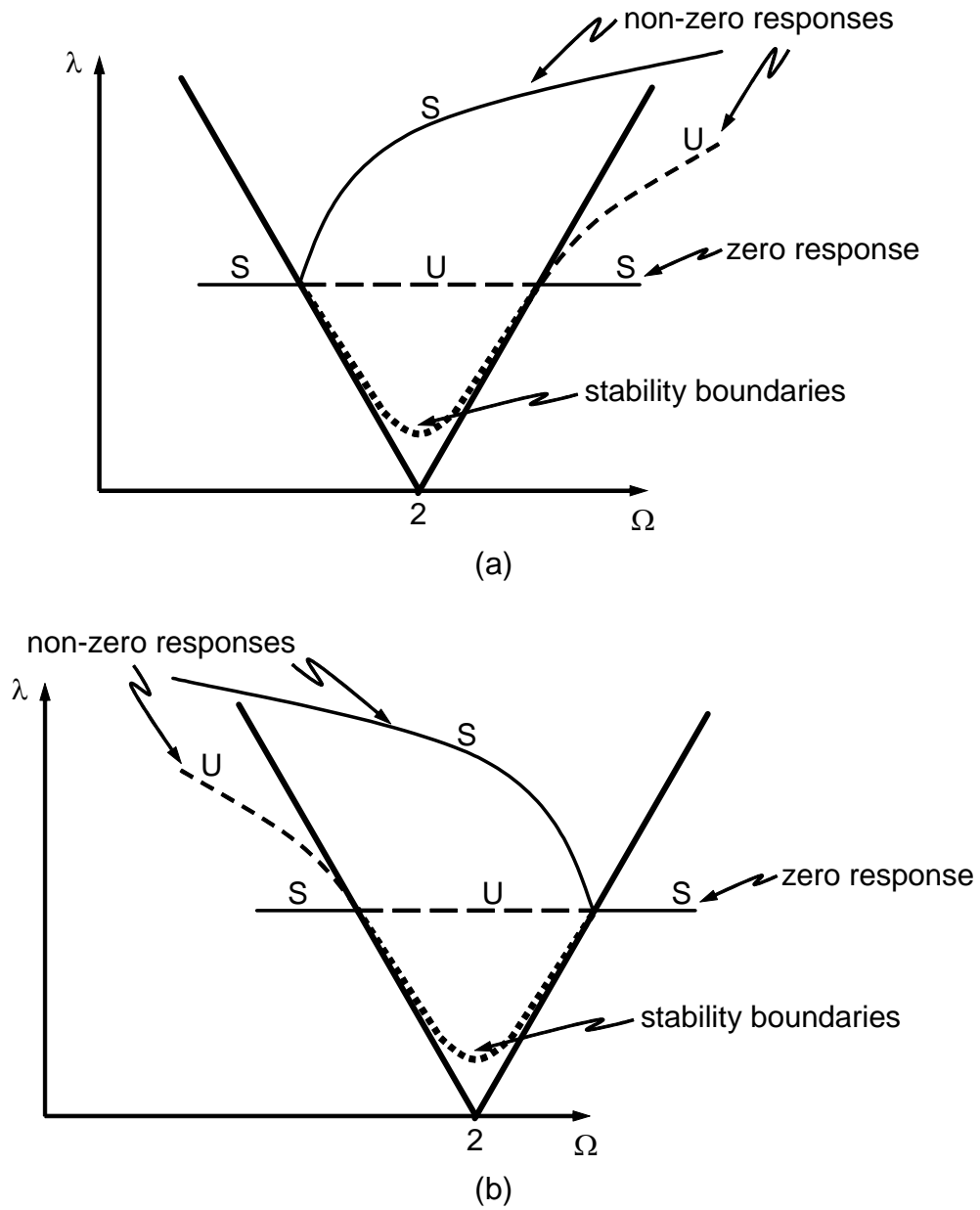


Figure 3. The dominant instability zone in the $\Omega - \lambda$ parameter space with a superimposed nonlinear frequency response for a given value of λ (Adapted from [4]); (a) with hardening nonlinearity ($\mu > 0$) (b) with softening nonlinearity ($\mu < 0$). Note that solid lines indicate a stable response and dashed lines indicate an unstable response. Also shown is the effect of damping on the instability region.

The resonant nature of a parametrically-excited system is also noteworthy. Unlike a directly-excited system, where small excitations produce resonant responses only when the forcing frequency is near the system's linear natural frequency, small excitations in a parametrically-excited system (including a Mathieu system) can produce resonant responses for other frequency conditions as well [35]. For example, if the excitation frequency is taken to be 2ω , parametric resonances can occur when the excitation frequency, ω , approaches ω_0 / n ($n = 1, 2, 3\dots$), where ω_0 is the linear natural frequency of the system. While the $n = 1$ resonance (primary parametric resonance) is by far the most common one encountered, higher order resonances do occur, although their appearance is heavily dependent on the amount of damping present in the system, due to the upward shifts mentioned above. These resonances appear only in lightly damped environments [45]. It should also be noted that due to the unique nature of parametric resonance, parametrically-excited systems exhibit quite abrupt transitions between trivial and nontrivial responses.

Due to the unique actuation methods and lightly damped environments inherent to MEM devices, parametric excitation and its associated resonances arise quite naturally in certain MEM oscillators. In particular, such phenomena have been observed in oscillators electrostatically driven by non-interdigitated comb drives (see Figure 4) [45-49]. Similar to their interdigitated counterparts, non-interdigitated comb drives utilize a voltage source to induce motion through electrostatic effects [5, 50, 51]. However, unlike interdigitated drives where the

motion induced is parallel to the ‘tines’ or ‘fingers’ of the comb, the motion induced by non-interdigitated drives is perpendicular to the ‘tines’; see Figure 4. More relevantly, under an alternating voltage input the non-interdigitated drives, through fringing electrical fields, produce a fluctuating electrostatic stiffness, which in turn results in a parametric excitation upon the oscillator [5]. Note that the excitation is purely parametric only if the tines are symmetrically aligned so that there is zero net force in the mechanical equilibrium state.

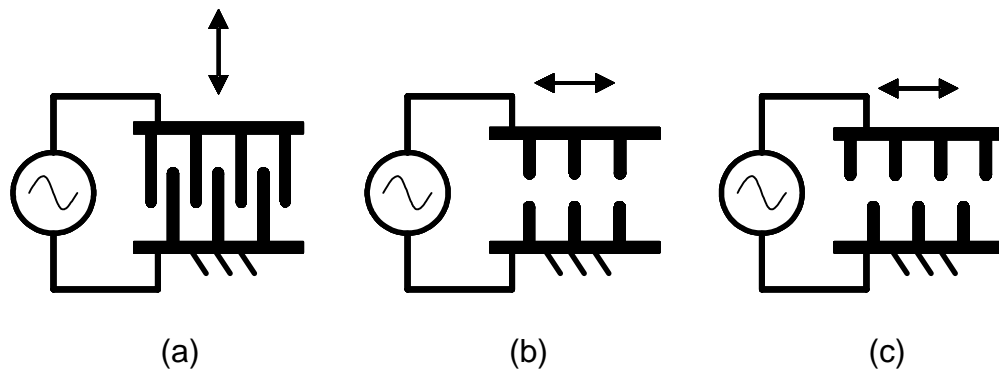


Figure 4. Schematic of both interdigitated and non-interdigitated electrostatic comb drives (Adapted from [5]). The arrows designate the dominant direction of motion. (a) An interdigitated comb drive. (b) A non-interdigitated comb drive in an ‘aligned’ position. (c) A non-interdigitated comb drive in a perfectly ‘misaligned’ position.

From a filtering point of view, the existence of parametric resonance in MEM oscillators is highly desirable for a few reasons. Namely, if the oscillator’s instability zones are exploited as passbands and the input of its AC comb drive is exploited as a system input, because of the abrupt on/off nature of parametric resonance, such oscillators, acting as filters, would exhibit nearly ideal stopband rejection and an extremely sharp response roll-off [1, 2]. However, these

benefits come at a cost, as the addition of parametric excitation (and the associated parametric instabilities) introduces a number of complications.

Among the most obvious complications are [1, 2]:

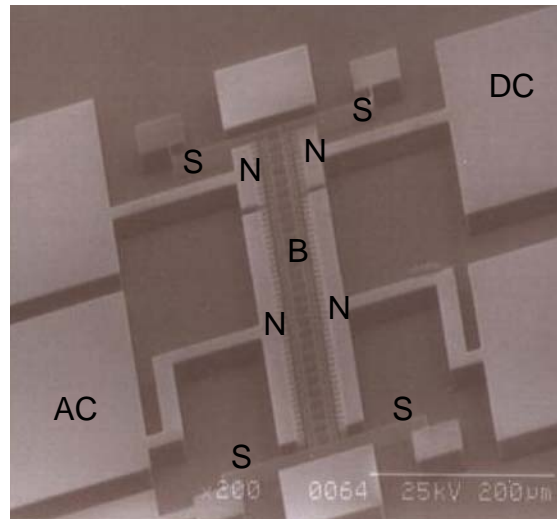
- The center frequency and bandwidth of the passband, or the center and width of the instability zone, depend on the amplitude of the excitation.
- Nontrivial responses can exist outside of the passband due to hysteresis.
- There is a nonlinear relationship between the system's input and output.
- Higher order resonances can occur.

Fortunately, these complications can be largely overcome through careful tuning and implementation of the oscillators, as presented in the forthcoming chapters.

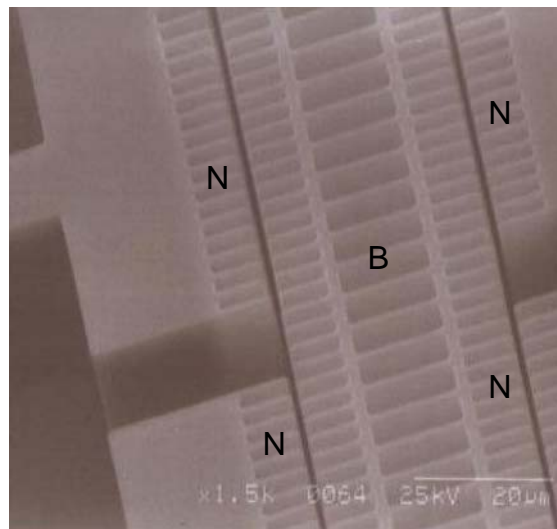
Chapter 4

The Dynamics of a Single Parametrically-Excited MEM Oscillator

In an attempt to gain a better understanding of the proposed bandpass filter design, its benefits, and how it is achieved in light of the shortcomings of the features of parametric resonance, consider a model for a single degree of freedom parametrically-excited MEM oscillator, such as that shown in Figures 5 and 6. This oscillator, similar to those oscillators examined in [1, 2, 4, 5, 52], but designed for the specific tuning characteristics required for a filter, consists of a shuttle mass, essentially the oscillator's backbone "B", anchored to a substrate by four folded-beam springs "S" and excited by two sets of non-interdigitated comb drives "N", which are individually powered by AC and DC voltage sources (for tuning purposes, as described subsequently).



(a)



(b)

Figure 5. (a) A representative parametrically-excited MEM oscillator [1]. The oscillator’s backbone “B” is the primary mass, the springs “S” provide attachment to ground as well as the mechanical restoring force, and the non-interdigitated comb drives “N” are used to provide parametric excitation. “AC” and “DC” indicate voltage sources. (b) A close up view of the non-interdigitated comb drives [1]. [Pictures courtesy of Barry Demartini and Dr. Kimberly Turner, University of California, Santa Barbara.]

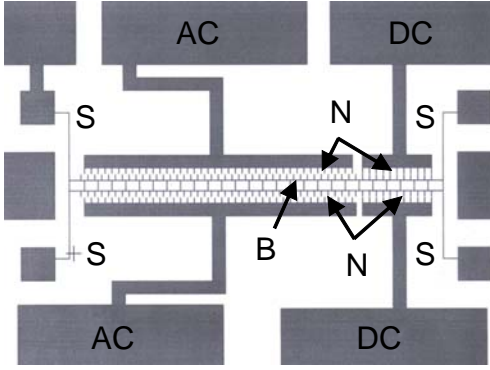


Figure 6. A CAD drawing of a representative MEM oscillator [1].

The equation of motion for this oscillator has been previously developed, and can be expressed as [1, 2, 4]:

$$m\ddot{x} + c\dot{x} + F_r(x) + F_{es}(x, t) = 0, \quad (4.1)$$

where the elastic restoring force from the springs, $F_r(x)$, is accurately modeled by a cubic function of displacement of the form,

$$F_r(x) = k_1x + k_3x^3, \quad (4.2)$$

which is, in general, mechanically hardening, that is, $k_3 > 0$. The electrostatic driving and restoring forces, $F_{es}(x, t)$, are generated by two independent non-interdigitated comb drives, as shown in Figures 5(a) and 5(b). One comb drive utilizes a DC input voltage of amplitude V_0 and the other a square-rooted voltage signal of the form

$$V(t) = V_A \sqrt{1 + \cos(\omega t)}, \quad (4.3)$$

which is used to ensure the isolation of harmonic and parametric effects [45]. As with the elastic restoring force, cubic functions of displacement provide an accurate model of the resulting force, which is also proportional to the square of the respective voltage signals [45]. Thus, the combined force from the two sets of comb drives can be expressed as

$$F_{es}(x, t) = (r_{10}x + r_{30}x^3)V_0^2 + (r_{1A}x + r_{3A}x^3)V_A^2(1 + \cos(\omega t)), \quad (4.4)$$

where r_{10} , r_{30} , r_{1A} , and r_{3A} are electrostatic coefficients that depend on the geometry of the comb drives. Substituting these forces into Equation 4.1 results in a net equation of motion for the shuttle mass, or the oscillator's backbone, of the form [1, 2]:

$$m\ddot{x} + c\dot{x} + k_1x + k_3x^3 + (r_{10}x + r_{30}x^3)V_0^2 + (r_{1A}x + r_{3A}x^3)V_A^2(1 + \cos(\omega t)) = 0. \quad (4.5)$$

To facilitate analysis this equation is nondimensionalized by rescaling time according to

$$\tau = \omega_0 t, \quad (4.6)$$

where ω_0 is the purely elastic natural frequency defined as,

$$\omega_0 = \sqrt{\frac{k_1}{m}}, \quad (4.7)$$

and rescaling displacement according to

$$\varepsilon^{1/2} \mathbf{z} = \frac{\mathbf{x}}{x_0}, \quad (4.8)$$

where x_0 is a characteristic length of the system (e.g. the length of the oscillator's backbone) and ε is a scaling parameter introduced to aid the analysis. This results in a nondimensional equation of motion of the form

$$\mathbf{z}'' + 2\varepsilon\zeta\mathbf{z}' + \mathbf{z}(1 + \varepsilon\nu_1 + \varepsilon\lambda_1 \cos(\Omega\tau)) + \varepsilon\mathbf{z}^3(\chi + \nu_3 + \lambda_3 \cos(\Omega\tau)) = 0, \quad (4.9)$$

where the new derivative operator and the nondimensional parameters are defined as in Table 1 [1, 2]. Note that by introducing the scaling parameter, ε , small damping and small parametric excitation have been assumed, which are consistent with the operation of MEM oscillators, especially near resonance [1]. It is also important to note that due to the tunable nature of MEM oscillators, many of the parameters present in Equation 4.9 can be specified through the design of the oscillator and the associated comb drives, or even tuned "on the fly" [1]. However, it should be noted that V_A and V_0 appear in many terms and this

imposes constraints on how the parameters are selected (In fact, this complication is the focus of the tuning in Chapters 5 and 6). For the present study, two sets of parameter values are used, as listed in Table 2 (their $\rho = \pm 1/2$ designations will become evident subsequently). Note that these parameters are taken from preliminary designs of a device similar to that shown in Figure 5.

Definition	Nondimensional Parameter
$(\bullet)' = \frac{d(\bullet)}{d\tau}$	Scaled Time Derivative
$\varepsilon\zeta = \frac{c}{2m\omega_0}$	Scaled Damping Ratio
$\varepsilon\nu_1 = \frac{r_{10}V_0^2 + r_{1A}V_A^2}{k_1}$	Linear Electrostatic Stiffness Coefficient
$\varepsilon\lambda_1 = \frac{r_{1A}V_A^2}{k_1}$	Linear Electrostatic Excitation Amplitude
$\Omega = \frac{\omega}{\omega_0}$	Nondimensional Excitation Frequency
$\chi = \frac{k_3x_0^2}{k_1}$	Nonlinear Mechanical Stiffness Coefficient
$\nu_3 = \frac{x_0^2(r_{30}V_0^2 + r_{3A}V_A^2)}{k_1}$	Nonlinear Electrostatic Stiffness Coefficient
$\lambda_3 = \frac{x_0^2r_{3A}V_A^2}{k_1}$	Nonlinear Electrostatic Excitation Amplitude

Table 1. Nondimensional parameter definitions [1, 2].

$\rho = 1/2$ Oscillator	$\rho = -1/2$ Oscillator
$k_1 = 10 \mu\text{N}/\mu\text{m}$	$k_1 = 10 \mu\text{N}/\mu\text{m}$
$k_3 = 0.05 \mu\text{N}/\mu\text{m}^3$	$k_3 = 0.05 \mu\text{N}/\mu\text{m}^3$
$x_0 = 1 \mu\text{m}$	$x_0 = 1 \mu\text{m}$
$m = 4.0528\text{E-}10 \text{ kg}$	$m = 4.0528\text{E-}10 \text{ kg}$
$\zeta = 0.01$	$\zeta = 0.01$
$r_{1A} = 2\text{E-}3 \mu\text{N}/\mu\text{mV}^2$	$r_{1A} = 2\text{E-}3 \mu\text{N}/\mu\text{mV}^2$
$r_{10} = -5\text{E-}4 \mu\text{N}/\mu\text{mV}^2$	$r_{10} = -5\text{E-}4 \mu\text{N}/\mu\text{mV}^2$
$r_{3A} = 1\text{E-}3 \mu\text{N}/\mu\text{m}^3\text{V}^2$	$r_{3A} = 1\text{E-}3 \mu\text{N}/\mu\text{m}^3\text{V}^2$
$r_{30} = -2.5\text{E-}4 \mu\text{N}/\mu\text{m}^3\text{V}^2$	$r_{30} = -7.5\text{E-}4 \mu\text{N}/\mu\text{m}^3\text{V}^2$

Table 2. A comprehensive list of the design parameter used throughout this work [1].

Once nondimensionalized, the equation of motion presented in Equation 4.9 provides a foundation for the analysis of the MEM oscillator's response, especially with regard to varying physical parameters and system inputs. It is important to note that Equation 4.9 is not the typical nonlinear Mathieu equation, due to the presence of parametric excitation acting on the cubic term. While this significantly complicates the oscillator's response, as described in Chapter 6, it has no effect on the linear stability of the system's trivial response. As such, the stability characteristics of the trivial response are compatible with those outlined in Chapter 3. To confirm this, the averaged equations (derived in Chapter 6) can be used to analytically approximate the first instability zone for the oscillator's trivial response. This is shown in Figures 7(a) and 7(b) in terms of the $V_A - \Omega$ parameter space, that is, the physical excitation amplitude (the alternating voltage amplitude) versus nondimensional excitation frequency parameter space,

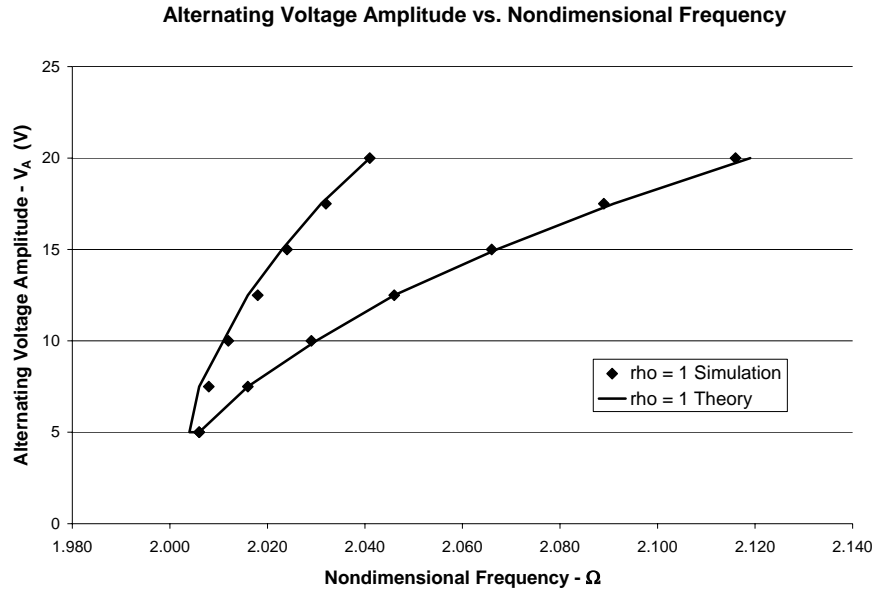
for both pure AC voltage excitation (Figure 7(a)) and a reference case which results in a symmetric wedge of instability (Figure 7(b)) achieved by a means described in Chapter 5. The amplitude-dependent critical frequency values are denoted Ω_{C1} and Ω_{C2} , such that the zero response is unstable in the range $\Omega_{C2} < \Omega < \Omega_{C1}$ (for $\lambda_1 > 0$). Using perturbation methods (see Chapters 5 and 6) these can be shown to be

$$\Omega_{C1} = 2 + \varepsilon \left(\nu_1 + \frac{\lambda_1}{2} \right) \quad (4.10)$$

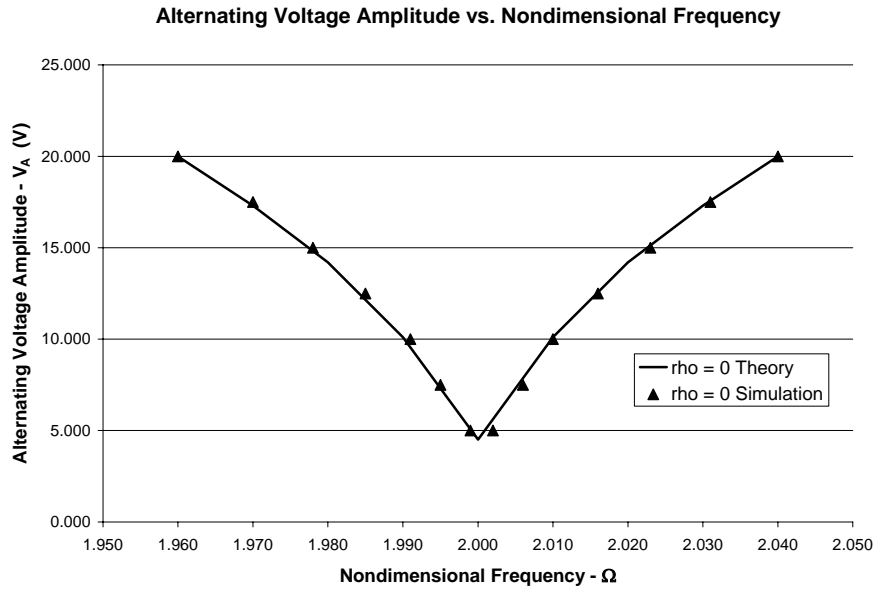
and

$$\Omega_{C2} = 2 + \varepsilon \left(\nu_1 - \frac{\lambda_1}{2} \right), \quad (4.11)$$

respectively. Also note that the accuracy of the analytical predictions has been verified with results from simulations of the full equation of motion, from which the stability boundary is determined by examining the behavior (growth or decay) of small perturbations from the oscillator's trivial response. The following section examines the critical features of the instability region.



(a)



(b)

Figure 7. The regions of parametric instability in the $V_A - \Omega$ parameter space produced using both the system's averaged equations and simulations of the system's full equation of motion with the linear parameters defined in Table 2. (a) The case of pure AC voltage excitation. (b) A nominal case which results in a symmetric wedge of instability [1].

Due to the nature of the filtering approach proposed in this work, the instability zones depicted in Figure 7 are of particular interest. Analogous to the instability zone emanating from $\Omega = 2$ in Figure 2, these “wedges of instability” exhibit stability characteristics very similar to those presented in Chapter 3. In fact, the only noticeable difference is that, unlike the primary instability zone shown in Figure 2, which features a constant center frequency and nearly linear transition curves, the center frequency and the transition curves in Figure 7 have a distinct curvature since the excitation amplitude is V_A^2 and the oscillator’s natural frequency depends on the square of the input voltage amplitudes, namely

$$\omega_n^2 = \frac{k_1 + r_{10}V_0^2 + r_{1A}V_A^2}{m}. \quad (4.12)$$

As explained in Chapter 3, inside the instability zone the trivial response is unstable, which results in a non-zero response that is dictated by the nonlinearities present in the system. Outside of the boundary, the trivial response is stable. This, however, does not ensure a zero response outside of the wedge, since the system can have multiple possible steady states, and nontrivial responses can occur outside of the instability zone, as thoroughly investigate in Chapter 6. This leads to potential hysteresis in the response, which is highly undesirable in a filter. Another characteristic to note is that the base of the instability wedge originates at the nondimensional frequency of 2, and therefore filtering takes place at twice the oscillator’s natural frequency, that is, at twice the frequency of filters which utilize direct excitation [1, 2]. The effect

of damping on this instability zone is also similar to the results presented in Chapter 3. Namely, the height of the instability zone's origin is dictated in a sensitive manner by the amount of aerodynamic and structural damping present in the system [1, 2]. As such, there is a critical AC voltage input required for the system to oscillate. This, however, is of minimal concern since the oscillators typically act in an environment with extremely low damping (near vacuum for testing) where Q factors can range into the thousands. In addition, the input (excitation) signal can be amplified, if needed, to attain the critical excitation amplitude. Finally, the amplitude-dependent nature of the stability boundary should be noted. A direct result of these facts is that the both bandwidth and center frequency of the system depend on the excitation amplitude, one of the primary drawbacks discussed in Chapter 3. The bandwidth deficiency is considered in the following chapter, while the hysteresis mentioned above is covered in Chapter 6 and the center frequency shift is discussed in Chapter 7.

Chapter 5

Linear Tuning: Manipulating the Instability Zone

As Figure 6 shows, the oscillator's activation frequencies (where the trivial solution undergoes a stability change) are strongly dependent on V_A , the amplitude of the AC voltage input. As such, when an untuned oscillator is employed as a filter, its bandwidth will be dependent on the excitation amplitude. However, it is possible to partially negate this effect through the implementation of a specific linear tuning scheme, namely, one in which the natural frequency of the oscillator, ω_n , is made to be dependent on V_A through a tuning of the linear electrostatic stiffness coefficients [1, 2]. This is accomplished by selecting the DC voltage in the DC comb drive to be dependent on V_A , which is the amplitude of the AC voltage that acts on the AC comb drive. A description of this tuning, as well as the net results it produces are presented here. Note that the theoretical basis for this tuning is largely founded on the averaged equations derived in Chapter 6.

To begin, it should be recognized that the signal to be filtered is the AC signal, and that the DC signal has been introduced in this analysis solely for this linear tuning. The DC voltage is to be dictated by the amplitude of the AC signal as follows. A designer-specified constant of proportionality α is introduced that relates the amplitude of the DC and AC voltage amplitudes according to

$$V_0 = \alpha V_A, \quad (5.1)$$

which results in the redefined parameters given in Table 3. Substituting these parameters into Equation 4.9 results in a revised equation of motion given by

$$z'' + z = -\varepsilon(2\zeta z' + z\lambda_1(\rho + \cos(\Omega\tau)) + z^3(\chi + \nu_3 + \lambda_3 \cos(\Omega\tau))), \quad (5.2)$$

wherein a new tuning parameter, ρ , is introduced that relates the linear electrostatic stiffness coefficient to the linear excitation amplitude, according to

$$\rho = \frac{\nu_1}{\lambda_1} = 1 + \frac{r_{10}\alpha^2}{r_{1A}}. \quad (5.3)$$

The parameter ρ represents the net effect that the AC amplitude, expressed in terms of λ_1 , has on the natural frequency of the oscillator. Specifically,

$$\omega_n = \sqrt{1 + \varepsilon\rho\lambda_1} = \sqrt{1 + \varepsilon\nu_1}. \quad (5.4)$$

Definition	Nondimensional parameter
$\varepsilon v_1 = \left(\frac{r_{10}\alpha^2 + r_{1A}}{k_1} \right) V_A^2$	Linear Electrostatic Stiffness Coefficient
$v_3 = \left[\frac{x_0^2 (r_{30}\alpha^2 + r_{3A})}{k_1} \right] V_A^2$	Nonlinear Electrostatic Stiffness Coefficient

Table 3. Redefined nondimensional parameters [1, 2].

The instability zone can thus be distorted through variation of ρ , since this produces a change in the linear natural frequency of the oscillator in a manner that is dependent on the input amplitude, V_A , through λ_1 [1, 2]. This results in a rotation of the wedge of instability away from the reference configuration, here taken as the symmetric case corresponding to $\rho = 0$, as shown in Figure 7(b). In particular, for $r_{1A} > 0$, by selecting $\rho > 0$ the wedge will rotate clockwise, and by selecting $\rho < 0$ the wedge will rotate counterclockwise. Note that one has the ability to set ρ by designing the comb drives with the desired electrostatic characteristics and then specifying α accordingly. Also note that if one does not activate the set of DC combs, and simply drives the system in the common manner, this corresponds to $\rho = 1$, since $\alpha = 0$, as shown in Figure 7(a).

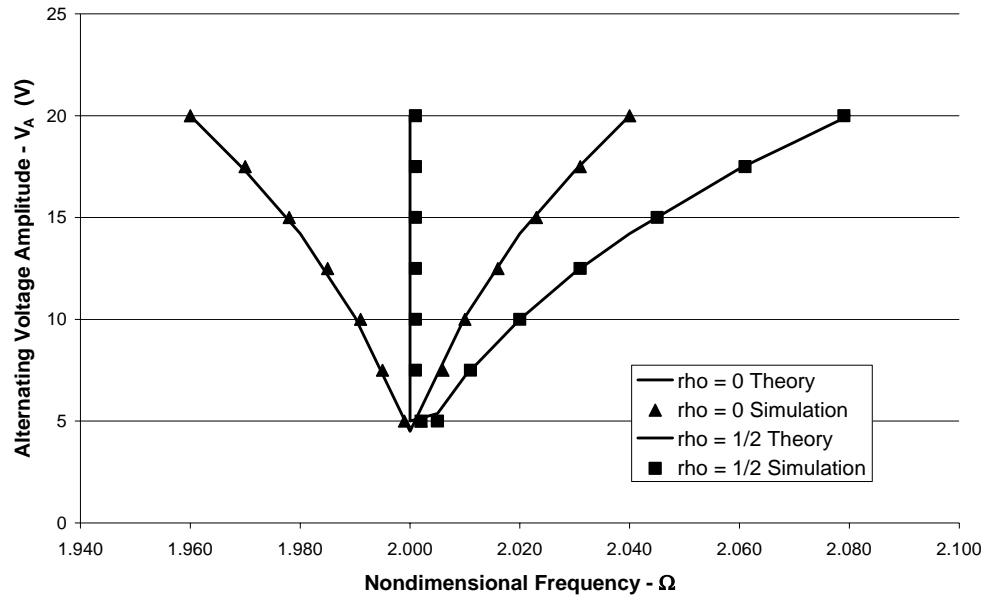
Using perturbation calculations (outlined in Chapter 6), it can be shown that by selecting $\rho = 1/2$ the left stability boundary of the wedge becomes vertical (to leading order in the perturbation calculations), as shown in Figure 8(a), and,

similarly, by selecting $\rho = -1/2$ the right stability boundary becomes vertical, as shown in Figure 8(b) [1, 2]. Higher order perturbation methods can be used to improve this verticality, however, the resulting improvement in performance is minimal, so nominal values of $\rho = \pm 1/2$ are used in this work. Note that the results described here correspond to $r_{1A} > 0$, the opposite trends in term of rotation occur for $r_{1A} < 0$.

The aforementioned verticality, achieved by selecting $\rho = \pm 1/2$, has the distinct advantage that it renders one of the oscillator's activation frequencies to be amplitude independent and, as such, makes it act essentially like a high or low pass switch. In particular, for $r_{1A} > 0$, by selecting $\rho = 1/2$, the oscillator will act as a high pass switch and by selecting $\rho = -1/2$ a low pass switch is achieved [1, 2].

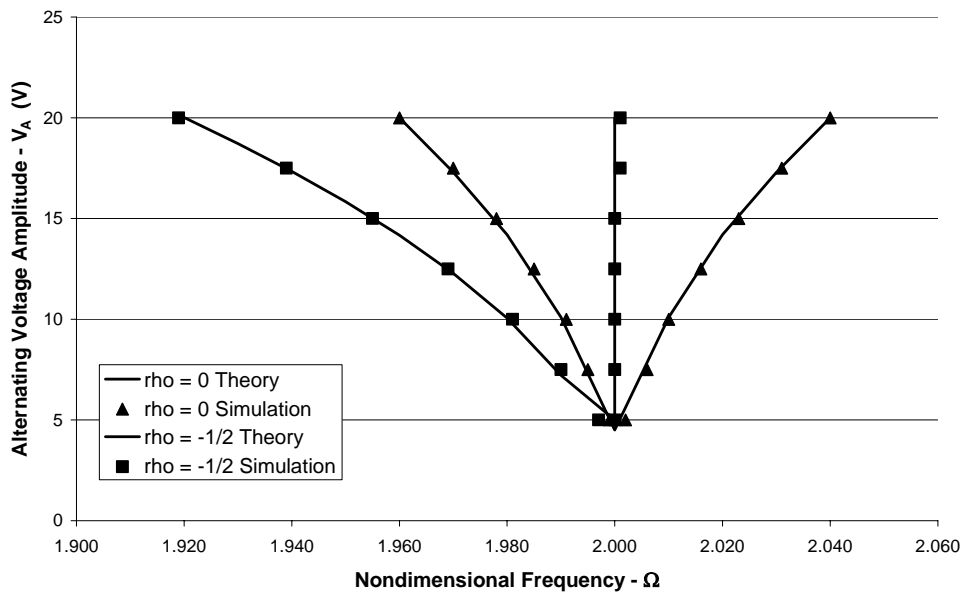
While this tuning provides a solution to one difficulty, others remain. The possible existence of nontrivial responses occurring outside of the instability zone is addressed in the next chapter.

Alternating Voltage Amplitude vs. Nondimensional Frequency



(a)

Alternating Voltage Amplitude vs. Nondimensional Frequency



(b)

Figure 8. Parametric instability zones in the $V_A - \Omega$ parameter space (for $r_{1A} > 0$) created using both analytical techniques and simulations. (a) $\rho = 0$ and $\rho = 1/2$. (b) $\rho = 0$ and $\rho = -1/2$.

Chapter 6

Nonlinear Tuning: Conditioning the Nontrivial Response

One deficiency of the tuned oscillators presented in Chapter 5 is that they have the propensity to feature non-zero response amplitudes outside of the wedge of instability, due to the presence of hysteresis in the system. However, the flexibility of the comb drives in these MEM devices allows one to adjust the system nonlinearities through electrostatic forces. Specifically, using well established techniques, the cubic nonlinearity produced by electrostatic effects in the comb drives can be tuned such that the oscillator's overall nonlinearity exhibits hardening, softening, or mixed hardening/softening characteristics [1, 2, 4-6, 52]. This can be verified by considering the effective nonlinearities of the MEM oscillator, as determined through a perturbation analysis, as follows.

6.1 Averaged Equations of Motion

To begin, Equation 5.2 is converted to the correct form for the application of the method of averaging by employing the standard coordinate transformation to amplitude and phase coordinates, specifically,

$$z(\tau) = a(\tau) \cos\left(\frac{\Omega\tau}{2} + \psi(\tau)\right), \quad (6.1)$$

$$z'(\tau) = -a(\tau) \frac{\Omega}{2} \sin\left(\frac{\Omega\tau}{2} + \psi(\tau)\right). \quad (6.2)$$

In order to capture the response near the primary parametric resonance, an excitation frequency detuning parameter, σ , is also introduced, defined by,

$$\Omega = 2 + \varepsilon\sigma, \quad (6.3)$$

in which σ measures the closeness of the excitation frequency to the principle parametric resonance condition. Equation 5.2 is then transformed to the amplitude/phase coordinates, $a(\tau)$ and $\psi(\tau)$, and the resulting equations that govern the dynamics of these variables are averaged over $4\pi / \Omega$ in the τ domain [1, 2, 6]. This results in the averaged equations

$$a' = \frac{1}{8} a \varepsilon \left[-8\zeta + (2\lambda_1 + a^2 \lambda_3) \sin(2\psi) \right] + O(\varepsilon^2) \quad (6.4)$$

$$\psi' = \frac{1}{8} \varepsilon \left[3a^2 (\chi + \nu_3) + 4\lambda_1 \rho - 4\sigma + 2(\lambda_1 + a^2 \lambda_3) \cos(2\psi) \right] + O(\varepsilon^2). \quad (6.5)$$

Note that the presence of the nonlinear electrostatic parametric excitation (λ_3) leads to a complicating term in the averaged equations, as compared to the usual nonlinear Mathieu equation. Consequently, the nontrivial steady-state solutions of the system take on a more complicated form, and the system has much more interesting response characteristics.

6.2 Analysis of the Steady-State Responses

Since the characteristic form of the system nonlinearity (e.g. hardening, softening, etc.) is the critical feature of the response for current purposes, and this is unaffected by damping, zero damping ($\zeta = 0$) is assumed in order to simplify the analysis. Examining the steady-state responses in this case, reveals that the response has three sets of nontrivial branches. The first two sets, which can be derived by setting the left hand sides of Equations 6.4 and 6.5 equal to zero, solving for the cosine and sine terms, and evoking the first Pythagorean Identity, appear in pairs with amplitudes given by

$$\bar{a}_1 = \pm \sqrt{\frac{4\sigma - 2\lambda_1(2\rho - 1)}{3(\chi + \nu_3) - 2\lambda_3}}, \quad (6.6)$$

$$\bar{a}_2 = \pm \sqrt{\frac{4\sigma - 2\lambda_1(2\rho + 1)}{3(\chi + \nu_3) + 2\lambda_3}}. \quad (6.7)$$

(Note that each +/- pair represents the same physical response; they appear this way due to the phase relation of this subharmonic response to the excitation [35]) For each of these solutions, the sign of the term under the square root determines the frequency ranges over which these branches are real, and thus physically meaningful. It should be noted that the stability of the $a = 0$ solution cannot be determined directly from the averaged equations in polar form, due to the fact that the phase is undefined at $a = 0$. However, one can determine the stability of the trivial response using Cartesian coordinates, or it can be inferred from the nontrivial responses in Equations 6.6 and 6.7, since the frequency (σ) values at which these branches become zero correspond to the stability limits of $a = 0$. Furthermore, it is found that the trivial response is unstable within the frequency domain bounded by the critical values given in Equations 4.10 and 4.11. It is also easily seen from Equations 6.6 and 6.7 that by selecting $\rho = \pm 1/2$ one can render one of the boundary frequencies (that is, the σ values) where a branch appears independent of the input amplitude λ_1 , leading to the desired rotation of wedges described in the previous chapter.

Of direct interest here is the role played by the nonlinearities, which differ for each of these frequency-dependent branches. To describe these effects, effective nonlinear coefficients γ_1 and γ_2 are defined that dictate the hardening or softening behavior of the branches. These coefficients are taken from the denominator of the expressions above and are given by

$$\gamma_1 = 3(\chi + \nu_3) - 2\lambda_3 \quad (6.8)$$

and

$$\gamma_2 = 3(\chi + \nu_3) + 2\lambda_3. \quad (6.9)$$

Selecting $\gamma_1 < 0$ and $\gamma_2 < 0$ locally results in the usual overall system softening nonlinearity. Likewise, selecting $\gamma_1 > 0$ and $\gamma_2 > 0$ locally results in an overall system hardening nonlinearity. However, due to the unusual nature of this oscillator, two mixed cases also exist, namely, $\gamma_1 > 0$ and $\gamma_2 < 0$, and $\gamma_1 < 0$ and $\gamma_2 > 0$, which correspond to the two branches bending toward or away from each other, as determined by the sign of λ_1 and the magnitude of ρ [6]. This result is summarized in the chart presented in Figure 9 which delineates the various response regions within the $\gamma_3 - \lambda_3$ parameter space, where,

$$\gamma_3 = \chi + \nu_3 \quad (6.10)$$

is the component of the cubic nonlinearity that does not multiply the time varying term $\cos(\Omega\tau)$ while λ_3 is the component that does multiply it. Note that the transitions (bifurcations) between response types occur when one or both of the effective nonlinearities equal zero.

The solutions in the third set of nontrivial responses are determined by examining the $\zeta = 0$ version of Equation 6.4. They have constant amplitude (for zero damping) and are given by

$$\bar{a}_3 = \pm \sqrt{\frac{-2\lambda_4}{\lambda_3}}. \quad (6.11)$$

These solutions are, however, of comparatively less importance from a filtering point of view due to the nature of their stability and range of existence (though from a nonlinear systems point of view they are quite interesting) [6].

The nonlinear coefficients λ_3 and γ_3 are related to the input voltage amplitudes (see Tables 1 and 2), and thus the nonlinear characteristics of the response can change as the input amplitude varies. This must be accounted for in the design of the oscillators and comb drives, and may limit the range of allowable AC input voltages for the resulting filter. The following discussion addresses the intricacies of the oscillator's overall frequency response, as well as the effective nonlinearities' dependence on the system's input voltage, and how these vary with system design parameters.

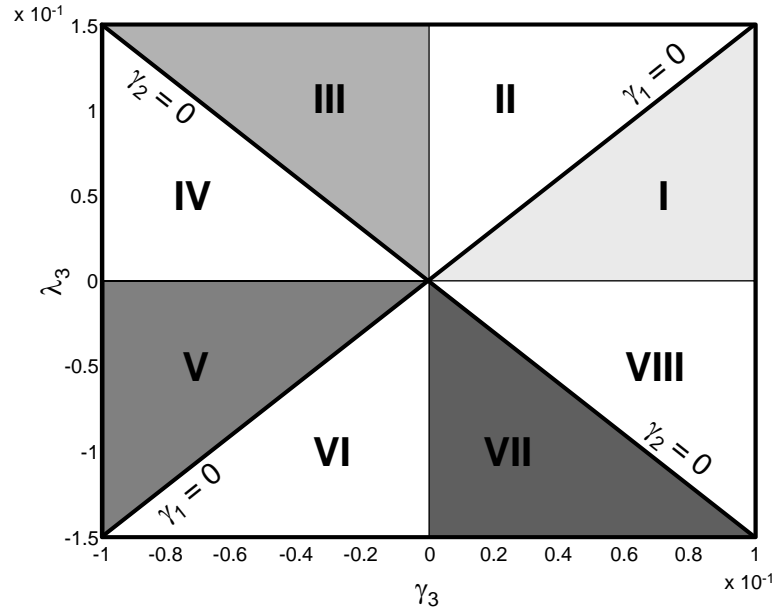


Figure 9. The $\gamma_3 - \lambda_3$ parameter space [6]. The roman numerals are used to designate the various response regions.

To facilitate further analysis of the oscillator's response and stability, the linear electrostatic stiffness coefficient is assumed to be zero ($\nu_1 = 0$, and thus $\rho = 0$), the linear electrostatic excitation amplitude, λ_1 , is taken to be positive, and damping is neglected. These assumptions introduce additional symmetries into the problem, which simplify the analysis of the system's various responses without compromising the applicability of the results to a more general system, i.e., the results provide an accurate "road map" for the overall response that is still qualitatively valid when the assumptions are relaxed. With these assumptions, frequency response curves (in terms of the detuning) are easily produced for parameter values within each of the eight response regions delineated in Figure 9. In order to obtain a complete picture, the stability of the response branches must be determined; this is considered next.

Though the local stability of steady-state responses is generally addressed by considering the local linear behavior of the averaged equations near the steady-state responses in the (a, ψ) polar coordinate space, singularities at the origin require that a coordinate change be introduced. As such, the following coordinate change is evoked, which converts the polar coordinates (a, ψ) into Cartesian coordinates (x, y) ,

$$x(\tau) = a(\tau) \cos[\psi(\tau)], \quad (6.12)$$

$$y(\tau) = a(\tau) \sin[\psi(\tau)]. \quad (6.13)$$

This coordinate change results in new averaged equations of the form [6]

$$x' = \frac{1}{8} \varepsilon [(2\lambda_1 + 4\sigma)y - 3\gamma_3 x^2 y + (-3\gamma_3 + 2\lambda_3)y^3 - 8\zeta x] + O(\varepsilon^2), \quad (6.14)$$

$$y' = \frac{1}{8} \varepsilon [(2\lambda_1 - 4\sigma)x + 3\gamma_3 x y^2 + (3\gamma_3 + 2\lambda_3)x^3 - 8\zeta y] + O(\varepsilon^2). \quad (6.15)$$

Using these equations, with $\zeta = 0$, local stability results are inferred by considering the response of the system when linearized about the steady states.

Letting

$$X(\tau) = \begin{bmatrix} x(\tau) \\ y(\tau) \end{bmatrix} \quad (6.16)$$

and

$$X^* = \begin{bmatrix} x^* \\ y^* \end{bmatrix}, \quad (6.17)$$

where the stars designate steady-state values, the local linearized equation of motion for the system can be written as

$$Y'(\tau) = J|_{X^*} Y(\tau), \quad (6.18)$$

where

$$Y(\tau) = X(\tau) - X^* \quad (6.19)$$

and J is the Jacobian matrix of the averaged equations presented above, Equations 6.14 and 6.15, evaluated at one of the system's steady states, X^* . The stability of the steady-state response is governed by the eigenvalues of the Jacobian matrix evaluated at the fixed points that correspond to the steady-state responses.

To simplify the analysis, we will consider the stability in terms of the trace and determinant of the Jacobian matrix [53]. This method proves to be sufficient due to the direct correlation between the eigenvalues of the Jacobian and its trace and determinant. In particular, the eigenvalues can be expressed in terms of the trace, T , and the determinant, Δ , as

$$\Lambda_{1,2} = \frac{1}{2} \left(T \pm \sqrt{T^2 - 4\Delta} \right). \quad (6.20)$$

For the undamped case under consideration here, the trace of the Jacobian for each of the steady-state responses is zero, thus only two equilibrium types are possible for nontrivial eigenvalues: saddles (unstable) and centers (marginally stable). Which of these two equilibrium types exists depends solely on the sign of the Jacobian's determinant. In particular, when $\Delta > 0$, the equilibrium will appear as a center, and when $\Delta < 0$, the equilibrium will appear as a saddle. The remaining case, $\Delta = 0$, corresponds to the case of two identically zero eigenvalues, and as such is used here only to calculate where stability changes occur.

The trivial solution features a determinant of the form

$$\Delta = -\frac{1}{16} \varepsilon^2 (\lambda_1^2 - 4\sigma^2). \quad (6.21)$$

By finding the roots of $\Delta = 0$, the critical frequency values (detuning values) at which stability changes occur can be shown to be

$$\sigma_1 = -\frac{\lambda_1}{2} \quad (6.22)$$

and

$$\sigma_2 = \frac{\lambda_1}{2} \quad (6.23)$$

respectively. The stability in each frequency (detuning) region is then determined by evaluating the determinant at a single point within the domain or by calculating the derivative of the determinant at the critical frequency value. As a quick computation will show, the trivial solution appears as a center for $\sigma < \sigma_1$ and $\sigma > \sigma_2$, and as a saddle for $\sigma_1 < \sigma < \sigma_2$. Using similar techniques the constant solutions of Equation 6.11 can be shown to be saddles for all frequency values where the solutions exists (determined by considering their phases), namely,

$$\min \left\{ \frac{\lambda_1}{2\lambda_3} (-3\gamma_3 \pm \lambda_3) \right\} < \sigma < \max \left\{ \frac{\lambda_1}{2\lambda_3} (-3\gamma_3 \pm \lambda_3) \right\}. \quad (6.24)$$

The two pair of nontrivial response branches are slightly more complicated in that their stability is heavily dependent on which region of the $\gamma_3 - \lambda_3$ parameter space (see Figure 9) the system falls within. Regardless, the stability for each of the branches can be found by evoking the fact that the response presented in Equation 6.6 has a determinant given by

$$\Delta = \frac{\varepsilon^2(\lambda_1 + 2\sigma)(3\lambda_1\gamma_3 - \lambda_1\lambda_3 + 2\lambda_3\sigma)}{4(3\gamma_3 - 2\lambda_3)}, \quad (6.25)$$

which features critical frequency values of

$$\sigma_1 = -\frac{\lambda_1}{2} \quad (6.26)$$

and

$$\sigma_2 = \frac{\lambda_1}{2\lambda_3}(-3\gamma_3 + \lambda_3), \quad (6.27)$$

and the response presented in Equation 6.7 has a determinant given by

$$\Delta = \frac{\varepsilon^2(\lambda_1 - 2\sigma)(3\lambda_1\gamma_3 + \lambda_1\lambda_3 + 2\lambda_3\sigma)}{4(3\gamma_3 + 2\lambda_3)}, \quad (6.28)$$

which features critical frequency values of

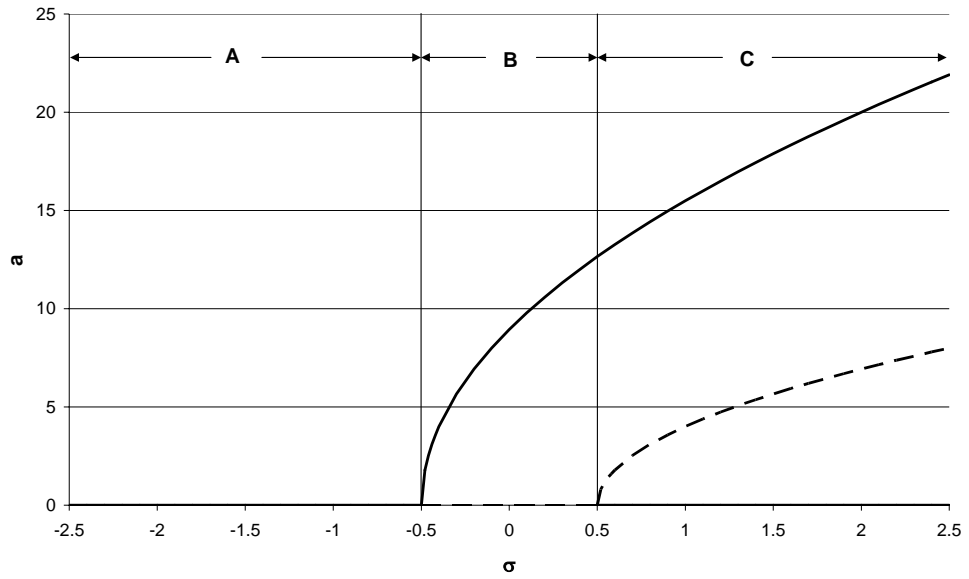
$$\sigma_1 = \frac{\lambda_1}{2\lambda_3}(-3\gamma_3 - \lambda_3) \quad (6.29)$$

and

$$\sigma_2 = \frac{\lambda_1}{2}. \quad (6.30)$$

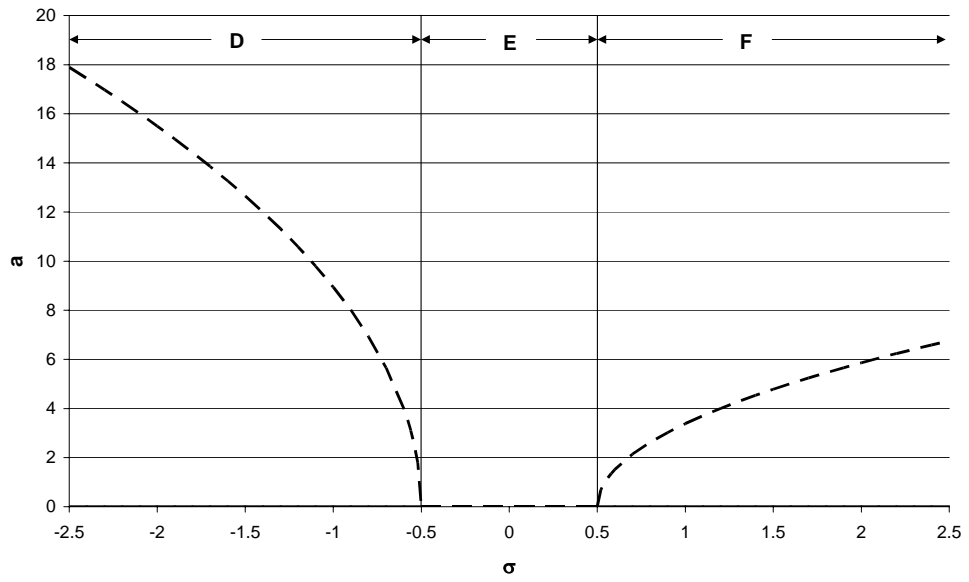
Combining each of these results with the steady-state solutions derived above yields a complete portrait of the oscillator's possible frequency responses, as shown in Figure 10.

Response Amplitude vs. Detuning in Region I ($\gamma_3 = 0.025, \lambda_3 = 0.025$)



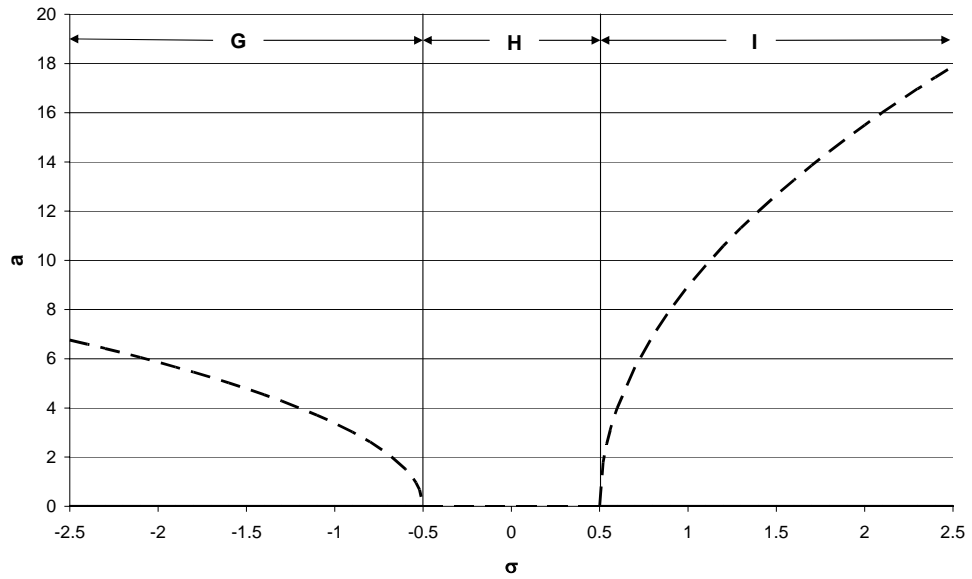
(a)

Response Amplitude vs. Detuning in Region II ($\gamma_3 = 0.025, \lambda_3 = 0.050$)



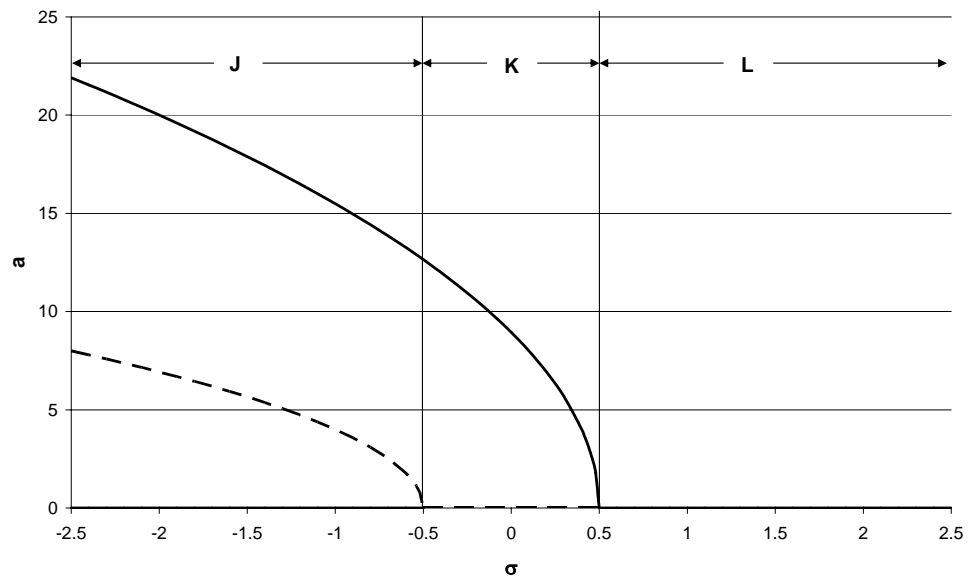
(b)

Response Amplitude vs. Detuning in Region III ($\gamma_3 = -0.025, \lambda_3 = 0.050$)



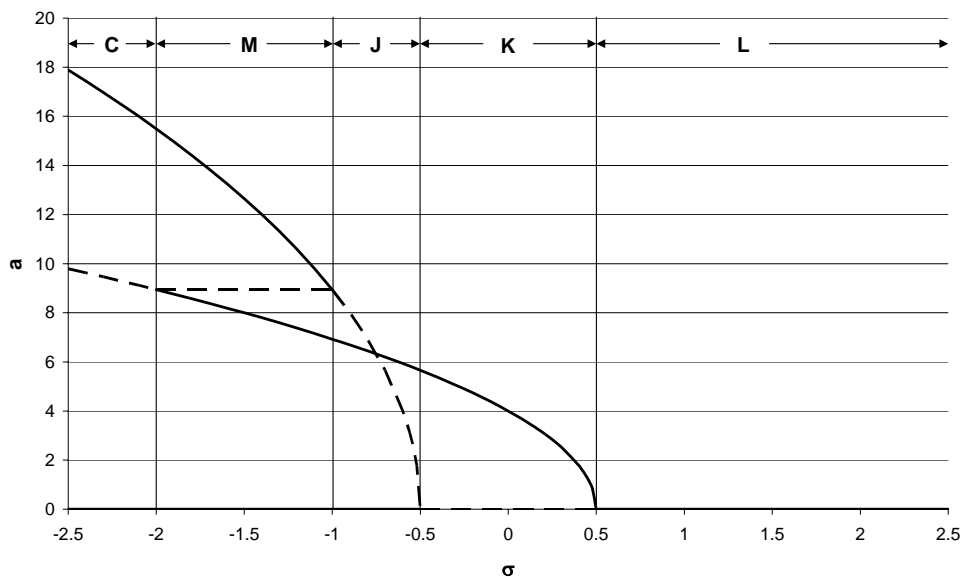
(c)

Response Amplitude vs. Detuning in Region IV ($\gamma_3 = -0.025, \lambda_3 = 0.025$)



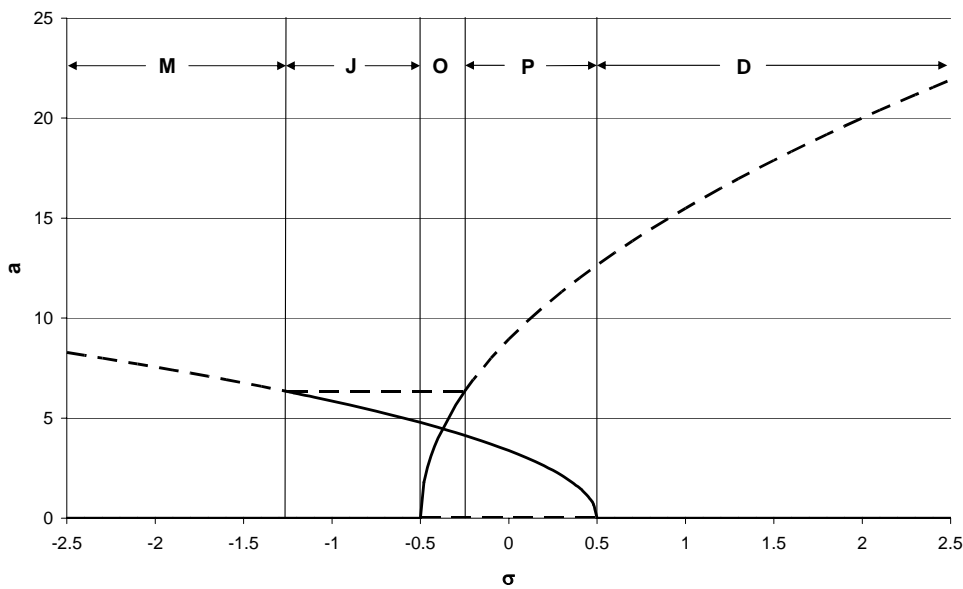
(d)

Response Amplitude vs. Detuning in Region V ($\gamma_3 = -0.025, \lambda_3 = -0.025$)



(e)

Response Amplitude vs. Detuning in Region VI ($\gamma_3 = -0.025, \lambda_3 = -0.050$)



(f)

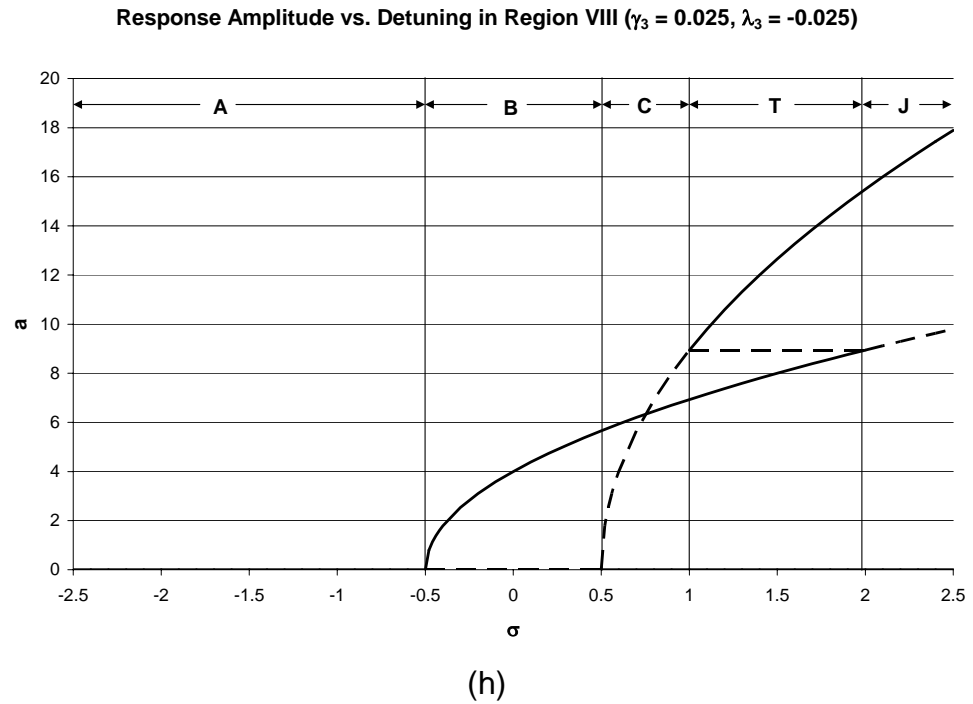
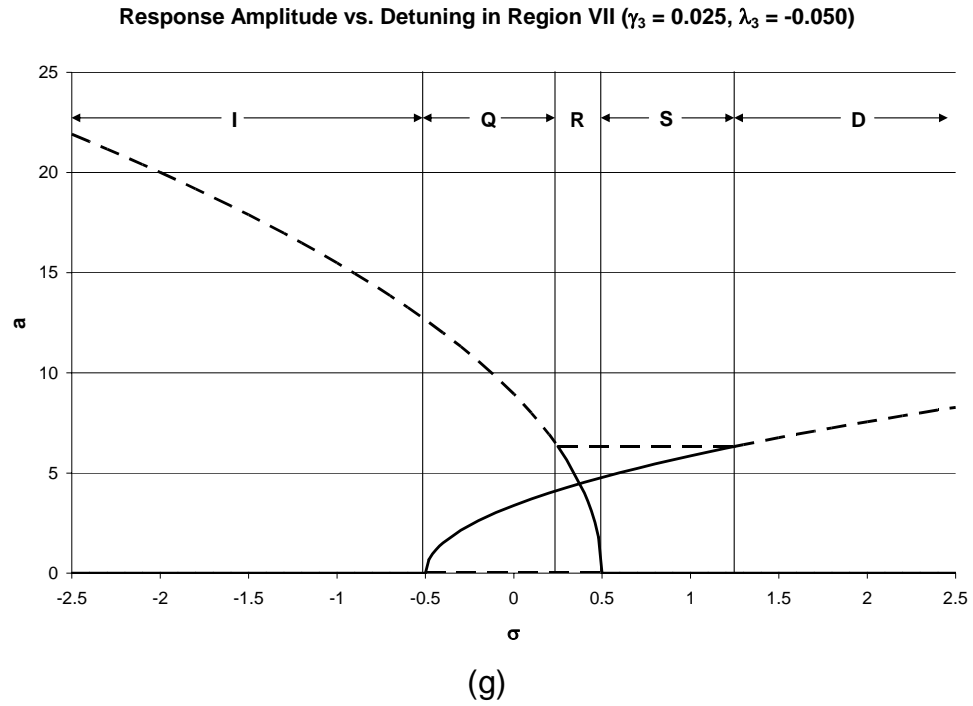


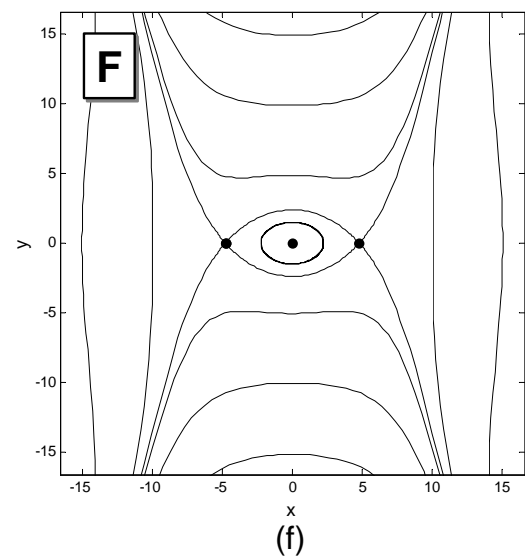
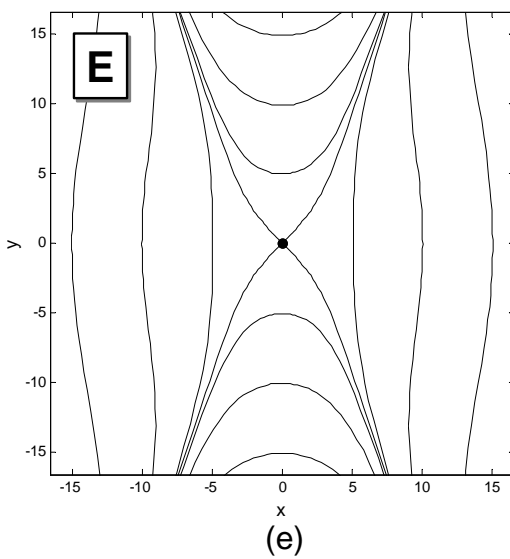
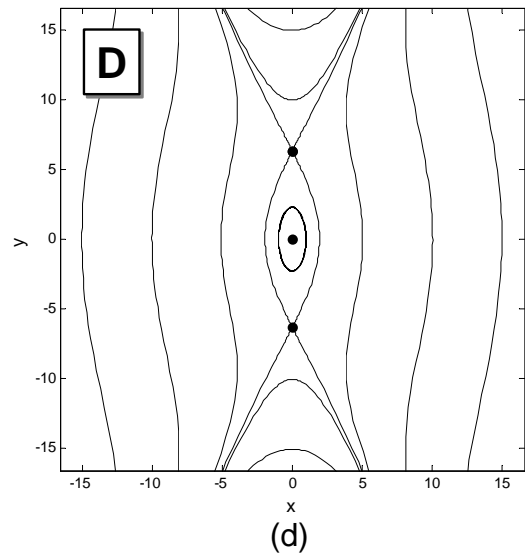
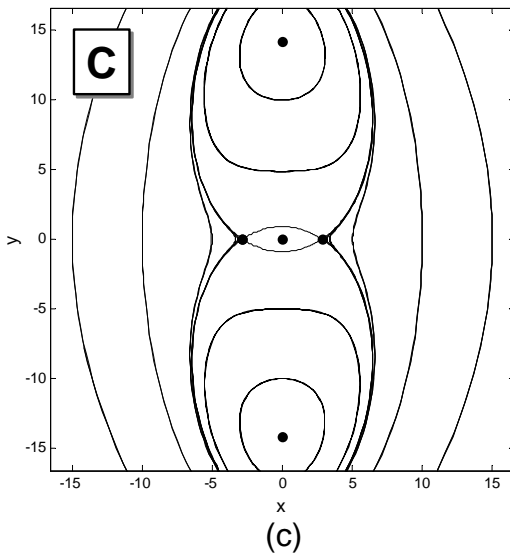
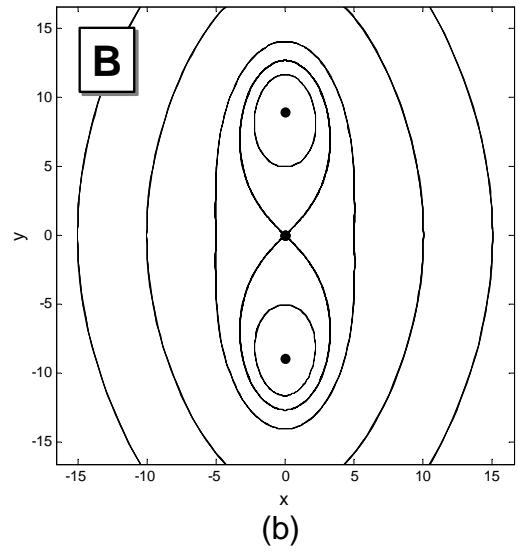
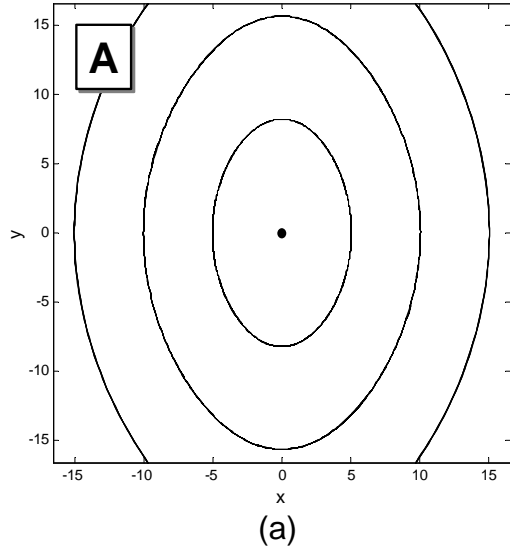
Figure 10. Representative frequency response plots showing response amplitude versus detuning frequency for each of the eight regions delineated in Figure 9 [6]. The frequency regions designated by the letters correspond to the phase portraits of Figure 11.

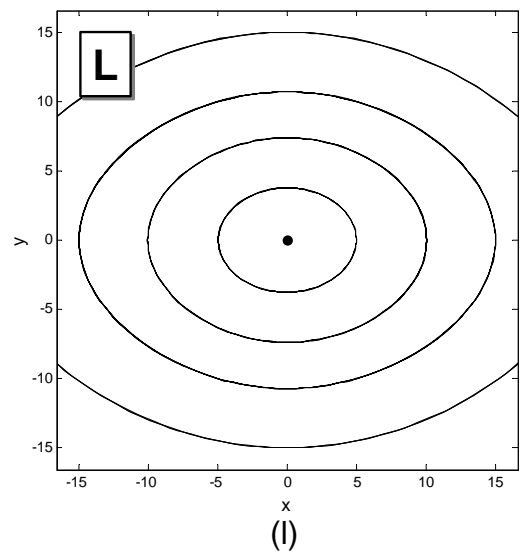
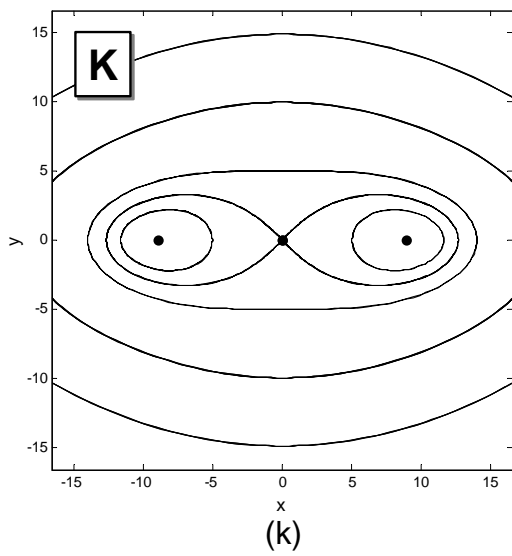
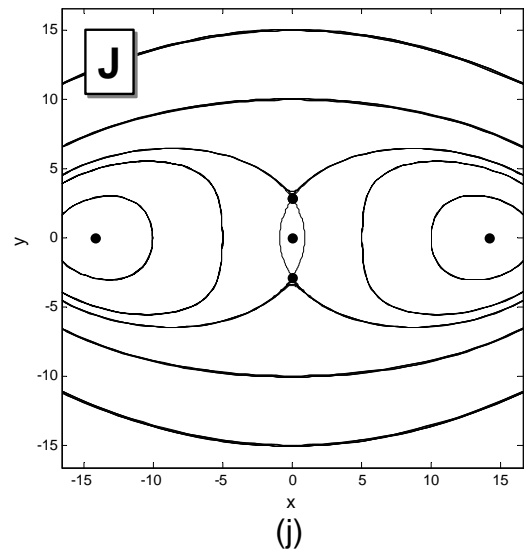
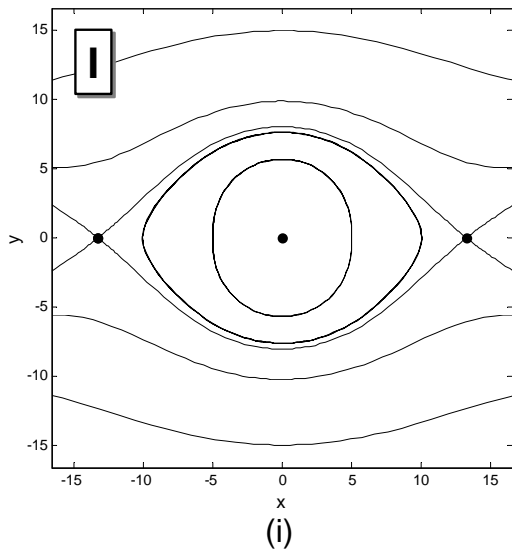
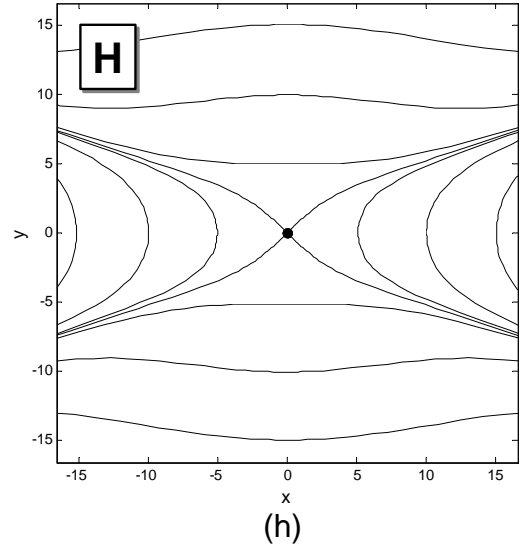
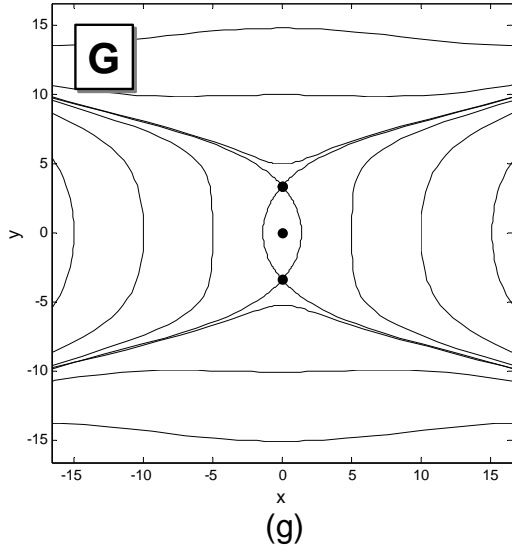
Due to the unique nature of many of the frequency response curves presented in Figure 10, each are briefly discussed here. To begin, the response curves depicted in Figures 10(a) and 10(d), corresponding to regions I and IV in Figure 9, are considered. As quick examination reveals, these regions appear consistent with normal softening and hardening nonlinear behavior. That is, the nontrivial solutions branch off in two distinct pitchfork bifurcations, one subcritical and the other supercritical, and all solutions remain globally bounded. The frequency responses shown in Figures 10(b) and 10(c), corresponding to topologically equivalent regions labeled II and III in Figure 9, are slightly more complicated. Here the nontrivial solutions also branch off, but in each instance a subcritical pitchfork bifurcation occurs. The net result is that the two response branches actually bend away from each other and some solutions are globally unbounded.

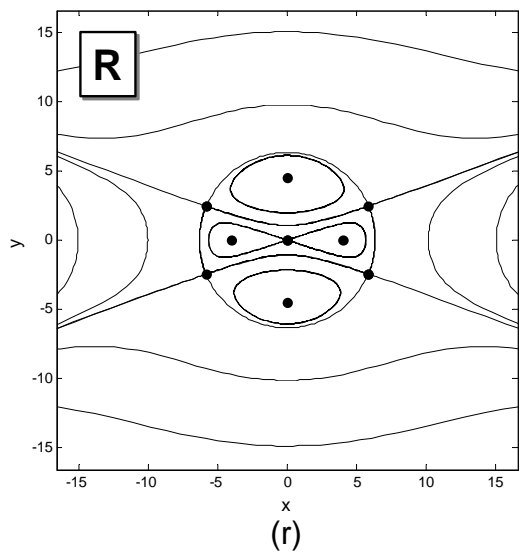
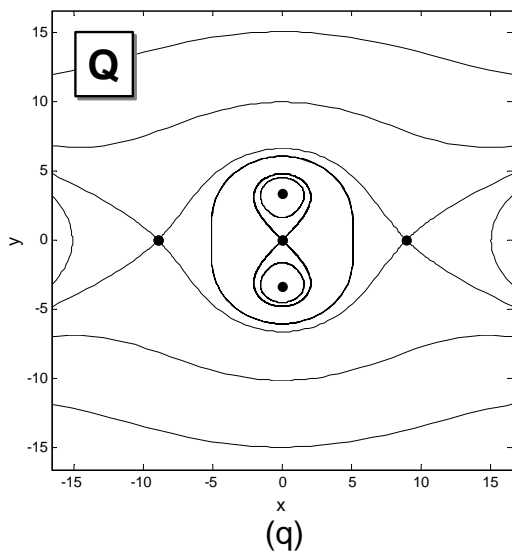
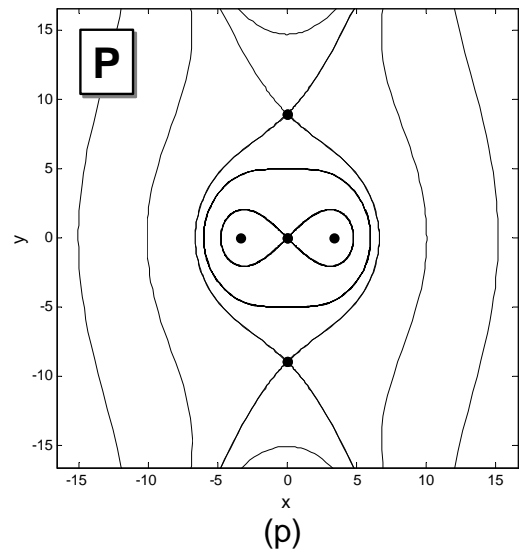
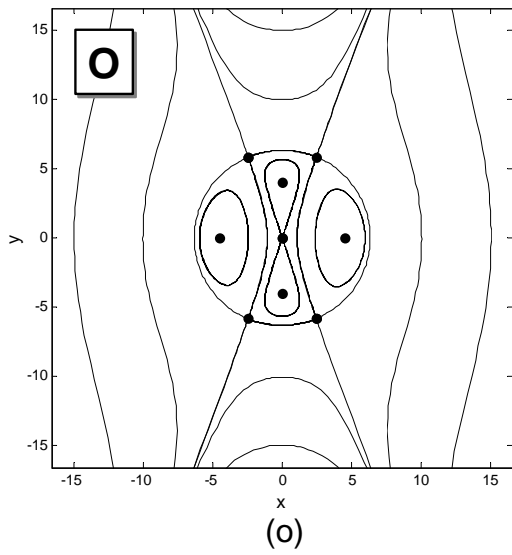
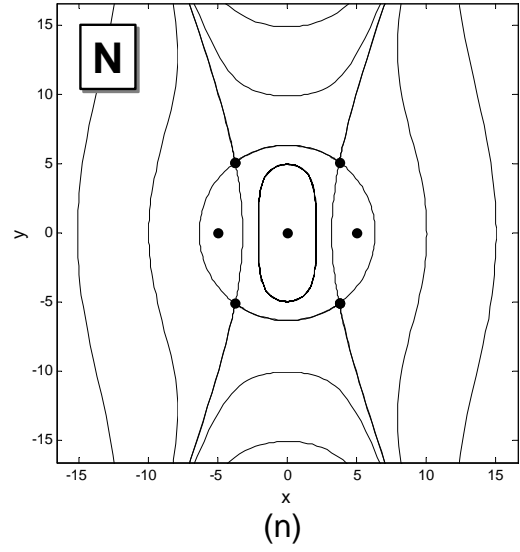
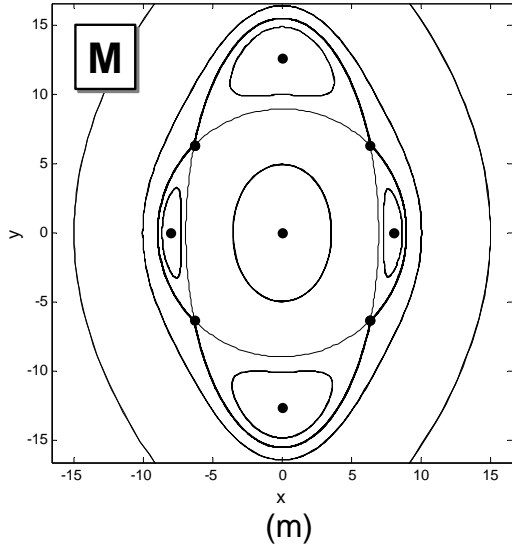
In the lower half-plane of the parameter space depicted in Figure 9, the existence of the additional nontrivial (constant amplitude) solution complicates matters. First, consider Figures 10(e) and 10(h), corresponding to regions V and VIII in Figure 9. Here the response locally resembles that of Figures 10(a) and 10(d). However, as the frequency is swept further away from zero detuning ($\sigma = 0$), the system undergoes two additional bifurcations, corresponding to the creation and annihilation of the constant amplitude response, which connects the other two nontrivial branches. Though this still results in a globally stable system

with quasi softening or hardening characteristics, it is distinct from the usual hardening and softening response curves of the upper half-plane, due to the fact that the stability in the two non-constant branches switches via the constant amplitude branch that connects them. The responses shown in Figures 10(f) and 10(g), corresponding to the regions labeled VI and VII in Figure 9, are also quite unique. Again, the responses feature four distinct bifurcations, two of the pitchfork variety where the nontrivial solution branches off from zero and two corresponding to the creation and annihilation of the constant amplitude solution, again connecting the other two nontrivial branches. The net result is a globally unstable system with nontrivial response branches which initially bend towards one another, are both initially stable, and lose stability via bifurcations with the constant amplitude branch.

To provide additional insight into the bifurcations described above, representative phase planes corresponding to each of the frequency regimes dictated in Figure 10 are depicted in Figure 11. Note that these phase planes are only the topological equivalent of those in the specified regimes, as many of the topologies occur in more than one set of response curves.







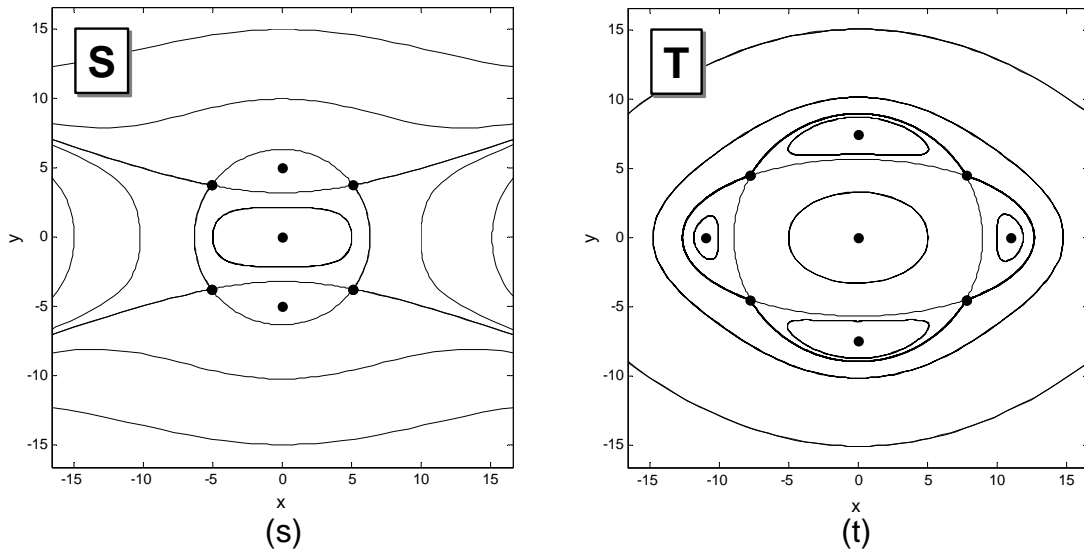


Figure 11. Representative phase plots corresponding to the frequency response regions defined in Figure 9 [6]. Solid dots indicate equilibrium points.

6.3 Tuning the MEM Oscillator's Nonlinearity

From a filtering point of view, the flexibility in selecting the nature of the nonlinearity is very useful for limiting the existence of non-zero solutions outside of, or at least on one side of, the instability zone. In particular, by specifying a hardening nonlinearity (Region I) or a quasi-hardening nonlinearity (Region VIII), that is $\gamma_1 > 0$ and $\gamma_2 > 0$, for a high pass switch ($\rho = 1/2$, for $r_{1A} > 0$), nontrivial responses below the activation frequency can be avoided [1]. Similarly, by specifying a softening nonlinearity (Region IV) or a quasi-softening nonlinearity (Region V), that is $\gamma_1 < 0$ and $\gamma_2 < 0$, for a low pass switch ($\rho = -1/2$, for $r_{1A} > 0$), nontrivial responses above the activation frequency can be avoided [1].

As alluded to earlier, this nonlinear tuning can be achieved through careful design of the comb drives [1]. Precise values of the effective nonlinear coefficients are not required, since one simply needs to ensure that hardening or softening (or even quasi-hardening or quasi-softening) persists, even in the face of the mechanical (hardening) nonlinearity and the AC input. Here r_{30} and r_{3A} , two parameters determined by the geometry of the fingers of the comb drives, must be selected such that the desired response characteristics are achieved over a given range of voltages. If this cannot be achieved in conjunction with the linear tuning constraints on r_{10} and r_{1A} , it would be possible to add an additional comb drive to the oscillator, whose sole purpose is to tune the nonlinearity. It should also be noted that since the mechanical nonlinearity is generally hardening, one will need significant electrostatic softening in the low pass switch in order to achieve overall softening over a reasonable range of voltages (this has recently been accomplished experimentally at UCSB [54]). Of course, maintaining the form of the nonlinearity is complicated significantly by the excitation amplitude (V_A) dependent nature of the system's nonlinearities, as examined next.

As shown in Tables 1 and 3, the nonlinear electrostatic terms that comprise the effective nonlinearities of the system, ν_3 and λ_3 , depend on the amplitude of the excitation voltage of the system, V_A . Accordingly, the system can actually transition from one response regime to another (in Figure 9) as the

amplitude of the alternating voltage changes. This can be confirmed by examining the form of the nonlinearity in the $\gamma_3 - \lambda_3$ parameter space. Taking the definitions of λ_3 and γ_3 ,

$$\lambda_3 = \frac{x_0^2 r_{3A} V_A^2}{k_1} \quad (6.31)$$

and

$$\gamma_3 = \chi + \nu_3 = \chi + \frac{x_0^2}{k_1} (r_{3A} + \alpha^2 r_{30}) V_A^2 \quad (6.32)$$

it is seen that at zero voltage the system starts at $(\gamma_3, \lambda_3) = (\chi, 0)$ (on the boundary between Regions I and VIII) and moves along a straight line in the $\gamma_3 - \lambda_3$ parameter space given by

$$\lambda_3 = \left(\frac{r_{3A}}{r_{3A} + \alpha^2 r_{30}} \right) (\gamma_3 - \chi) \quad (6.33)$$

as V_A is increased. To validate this consider the oscillator design designated $\rho = -1/2$ in Table 2. As Figure 12(a) shows, this oscillator's nonlinearity will move through regions I, II, III, and IV as the input voltage is varied from 0 to approximately 5 V. Similarly, the oscillator designated $\rho = 1/2$ in Table 2 will move through regions I and II as the input voltage is varied from 0 to

approximately 18 V, as shown in Figure 12(b). To avoid such transitions within a given oscillator's operating voltage range, consideration must be given to these effects during oscillator design. The following relationships are useful in determining the transition voltages, the critical voltage values corresponding to qualitative changes in the systems nonlinearity, for a given oscillator:

$$V_{A,C1} = \sqrt{\frac{-k_3}{r_{30}\alpha^2 + \frac{5}{3}r_{3A}}} \quad (6.34)$$

$$V_{A,C2} = \sqrt{\frac{-k_3}{r_{30}\alpha^2 + \frac{1}{3}r_{3A}}} \quad (6.35)$$

Note that to achieve an overall hardening behavior it is beneficial to have a hardening mechanical nonlinearity, as it ensures that a minimum voltage threshold will not be required to realize the desired nonlinearity. Likewise, it would be beneficial to have a softening mechanical nonlinearity in systems where an overall softening is desired. Unfortunately, this is not realizable in current designs, though it is currently being considered by the author. However, these systems will, due to the nature of the parametric resonance, have a threshold operating voltage in any case, and it has been experimentally observed that the transition from hardening to softening takes place at relatively low voltages [54].

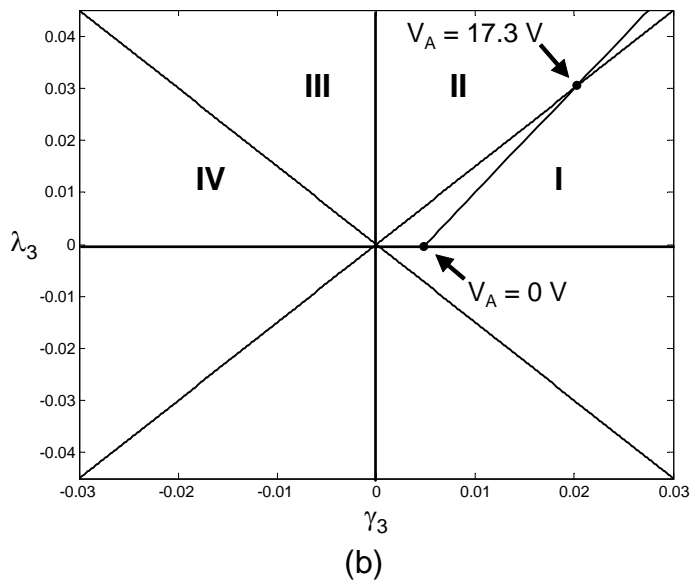
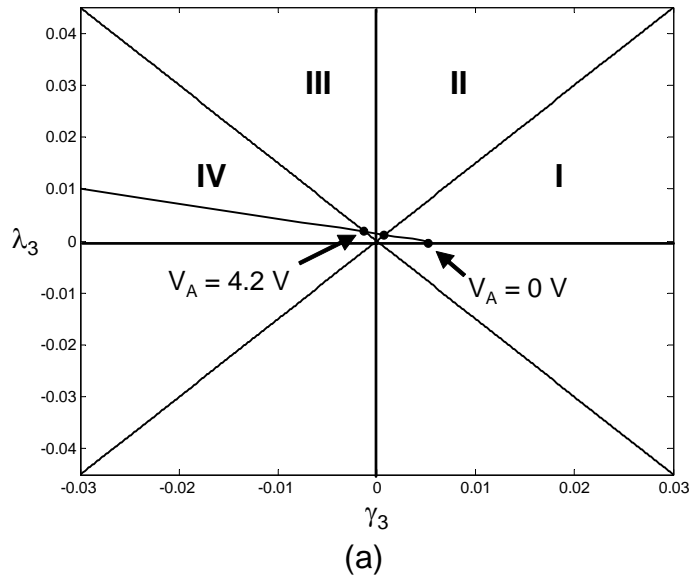


Figure 12. Sample parameter spaces showing how the oscillator's nonlinearity transitions between response regimes under a varying input excitation amplitude; (a) for the $\rho = -1/2$ design presented in Table 2, (b) for the $\rho = 1/2$ design presented in Table 2 [6].

6.4 Summary

The above analysis gives a quite complete picture of the response characteristics of the MEM oscillator of interest. For general parameter values (including the inclusion of damping) approximate response curves can be numerically produced from the averaged equations. Figure 13 highlights sets of curves for both a $\rho = 1/2$ oscillator with a hardening nonlinearity and a $\rho = -1/2$ oscillator with a softening nonlinearity. As predicted, each response curve originates at the chosen activation frequency ($\Omega = 2$) regardless of the AC excitation amplitude, V_A . This confirms that the instability wedges have been rotated as desired (see Figure 8). In addition, the response quickly increases from zero to a finite amplitude after activation. To confirm the validity of the perturbation calculations, results from numerical simulation of the full nonlinear equation of motion have also been included in Figures 8 and 13 [1]. Note that the averaged solutions provide excellent accuracy at low AC voltage amplitudes, and are reasonable at larger excitation voltages.

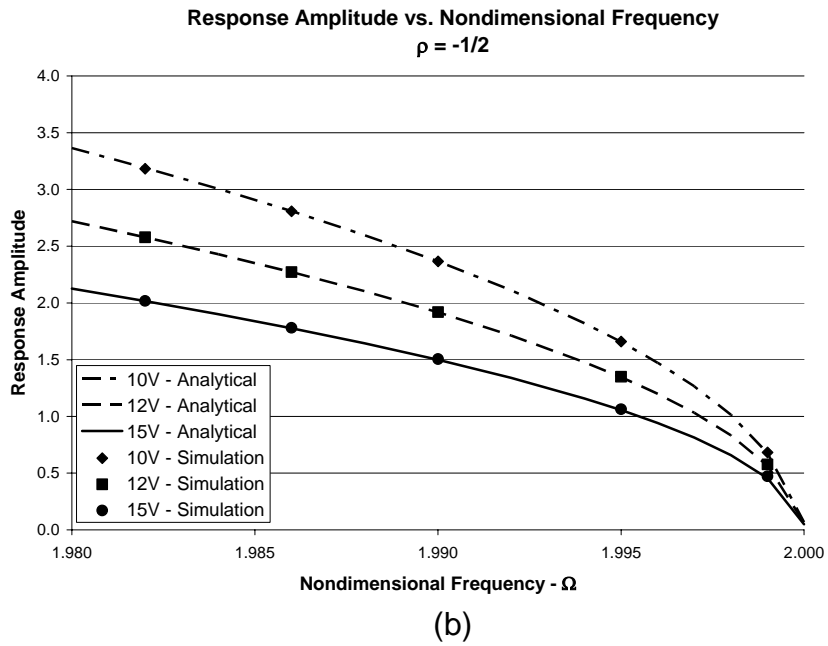
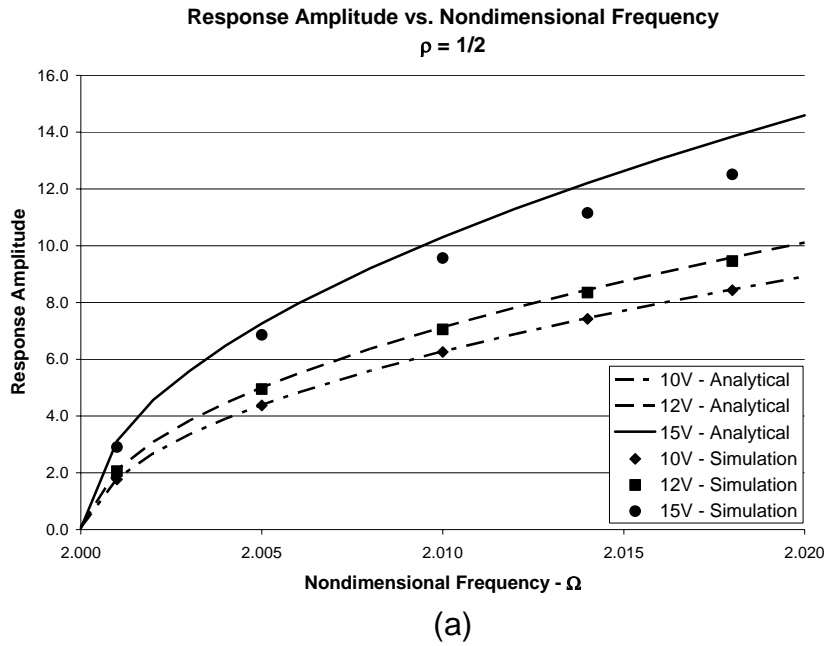


Figure 13. Sample response curves – amplitude vs. frequency: (a) $\rho = 1/2$ and (b) $\rho = -1/2$ [1].

Chapter 7

Creating a Bandpass Filter

While the tuning schemes presented in Chapters 5 and 6 effectively condition the response of an individual oscillator, they result in efficient frequency-activated switches, but not a bandpass filter [1, 2]. Furthermore, these switches are good at only one frequency, as the other instability boundary is still amplitude-dependent, and the responses will likely exhibit hysteresis beyond the switch point. However, two such oscillators, tuned to act as amplitude-independent switches at nearby frequency thresholds, have great potential for such use [1, 2]. In particular, it may be possible to create a bandpass filter through the implementation scheme shown in Figure 14.

The idea is to generate a bandpass filter which features a center passband frequency of Ω_0 and a bandwidth of $\Delta\Omega_0$, where Δ is defined to be a small parameter which describes the bandwidth as a percentage of the center frequency (see Figure 1). This parameter may also be used to define an “effective quality (Q) factor”, where Q_{eff} is independent of system damping, as follows,

$$Q_{eff} = \frac{1}{\Delta}. \quad (7.1)$$

To achieve this design, two oscillators are required. One is a high pass switch (with $\rho = 1/2$ for $r_{1A} > 0$) that has been nonlinearly tuned such that it exhibits a hardening nonlinearity, which will henceforth be designated as 'H'. The other is a low pass switch (with $\rho = -1/2$ for $r_{1A} > 0$) that has been nonlinearly tuned such that it exhibits a softening nonlinearity, which will henceforth be designated as 'L'. In addition, both the L and H oscillators must have their linear mechanical frequencies tuned such that the base points of their respective wedges of instability are slightly shifted from Ω_0 , so that the passband is created. This can be achieved by designing the oscillators so that their zero-voltage (i.e., purely mechanical) linear instability threshold frequencies are as follows: for the L oscillator the threshold is selected to be $\Delta\Omega_0/2$ above Ω_0 , and for the H oscillator the threshold is selected to be $\Delta\Omega_0/2$ below Ω_0 . With this, the oscillators' tuning is complete. A summary of the required tuning conditions for the two oscillators is given in Table 4.

Oscillator	Tuning	Condition
H Oscillator	Zero-Voltage Linear Frequency	$\omega_{0,H} = \sqrt{\frac{k_{1,H}}{m_H}} = \frac{\Omega_0}{2} \left(1 - \frac{\Delta}{2}\right)$
	Amplitude Dependent Linear Tuning ($\rho = 1/2$)	$\left(\frac{r_{10}\alpha^2}{r_{1A}}\right)_H = -\frac{1}{2}$
	Hardening Nonlinearity	Nonlinearity Region I or VIII
L Oscillator	Zero-Voltage Linear Frequency	$\omega_{0,L} = \sqrt{\frac{k_{1,L}}{m_L}} = \frac{\Omega_0}{2} \left(1 + \frac{\Delta}{2}\right)$
	Amplitude Dependent Linear Tuning ($\rho = -1/2$)	$\left(\frac{r_{10}\alpha^2}{r_{1A}}\right)_L = -\frac{3}{2}$
	Softening Nonlinearity	Nonlinearity Region IV or V

Table 4. Summary of tuning requirements for bandpass filtering [1]. The “Nonlinearity Region” refers to Figure 9.

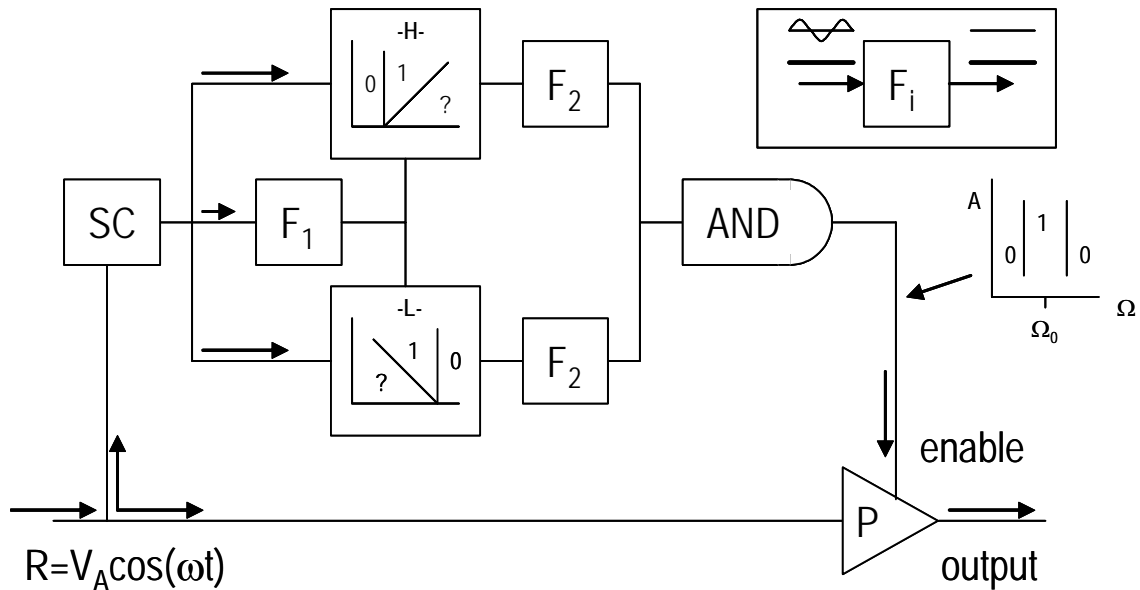


Figure 14. One proposed logic implementation scheme, which is capable of producing a bandpass filter [1, 2].

Once the two oscillators have been tuned in accordance with the conditions set forth in Table 4, they are ready for implementation in the filter system presented in Figure 14. This system is designed to function as follows. A harmonic input signal, R , of the form $R = V_I \cos(\omega t)$ is supplied to the system. This signal travels to a signal conditioner (SC) that produces an excitation signal appropriate for the oscillators' comb drives, namely the square-rooted input described in Chapter 4. This signal is then used to drive both the H and L oscillators, via the AC comb drives, and is also provided to the block designated F_1 . This block represents an AC to DC converter that produces the amplitude of R , namely V_I (which is monotonically related to V_A), or some proportion thereof. This DC signal is sent to the oscillators, where it is used to drive the two resonators, via the DC comb drives, and to tune each oscillator through their linear tuning parameters, $\rho = \pm 1/2$ (recall that the ρ tuning is set by α , which sets V_0 in relation to V_A .) Each oscillator, acting as described in previous sections, filters the provided input signal and acts as a switch, producing a zero (in practice, the noise floor) or finite amplitude oscillatory response, depending on the frequency of the excitation signal. The respective signal from each oscillator is then sent to another block designated F_2 which converts the signal into a constant voltage, or into a digital signal. For example, F_2 may produce a 0 when the oscillator's output is zero (noise floor) and 1 when the output is oscillating or, this is simply an AC to DC converter. The signal from each F_2 block then proceeds to an AND junction, which provides a non-zero signal to an enabling input of block P only when the frequency of the input signal falls within the

desired bandwidth. If the enabling input of device P receives a non-zero signal, it allows the original filter input to pass unimpeded; otherwise, it blocks the signal. The result is a bandpass filter with ideal stopband rejection and optimal roll-off in its frequency response.

To verify the operation of the filtering scheme presented in Figure 14, numerical simulations of the system were carried out using Simulink™ [55]. As Figure 15 shows, the results for a bandpass filter designed with an effective quality factor of 500 are essentially as expected. The filter's bandwidth and center frequency are nearly amplitude independent (note the horizontal scale), and could be made even more so by refining the tuning parameters, the ρ 's. In addition, the attenuation outside of the passband is absolute, which verifies that the filter's stopband rejection is ideal. Finally, the filtering takes place at twice the natural frequency of the system, or twice the frequency of those filters which utilize linear resonance.

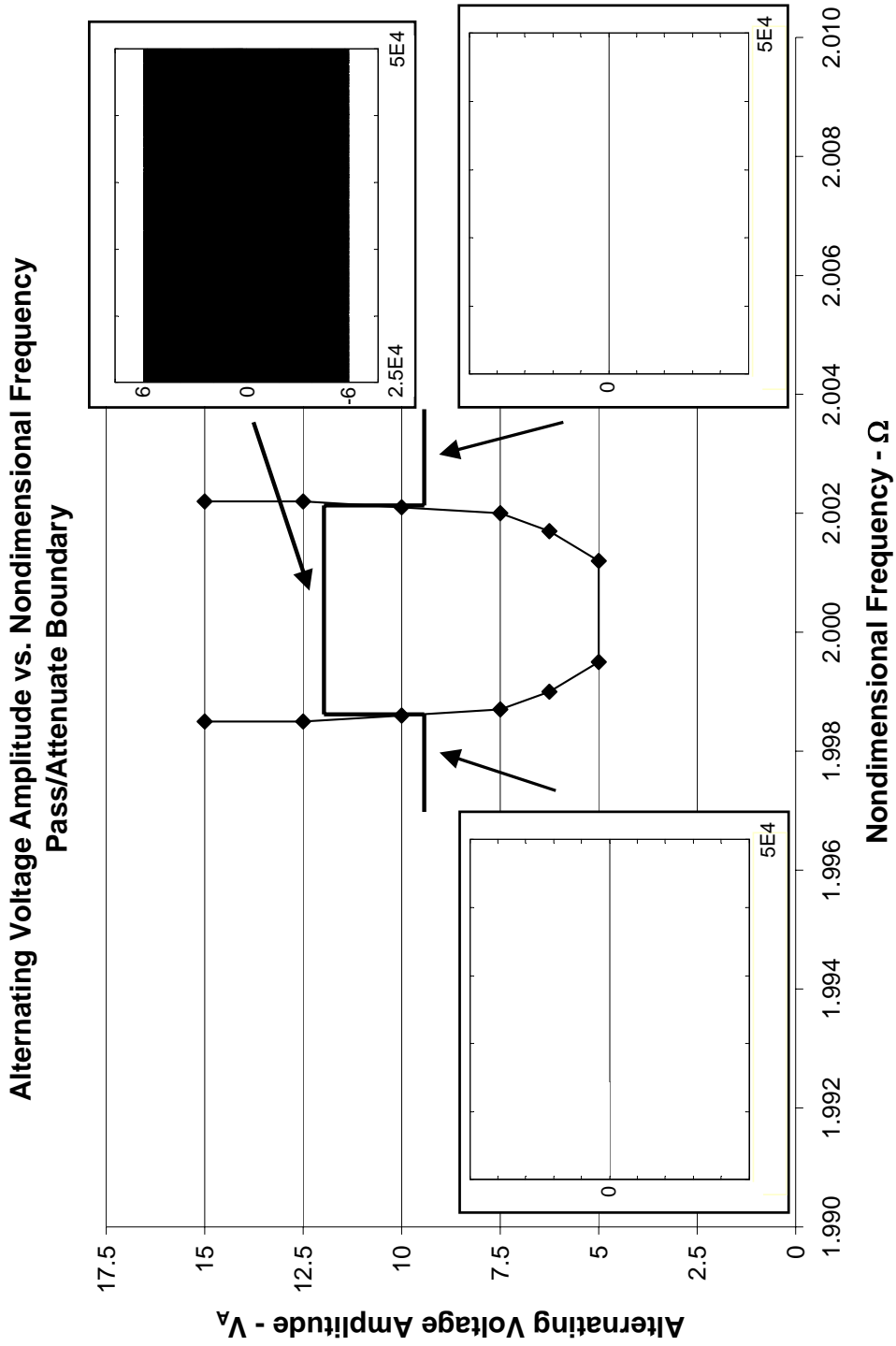


Figure 15. Simulation results from the filter system of Figure 14 [1]. Data points are frequency thresholds for the passband boundaries at various AC amplitude levels. The insets show the system steady-state time-domain outputs at the points indicated.

Chapter 8

Design Robustness Issues

So far, the discussion of filters within this work has been largely based on the assumption that the filters' input is both known and deterministic and that target values for design parameters are readily achievable. However, in practice uncertainties arising in both the system's input and design parameters must be characterized and addressed. In particular, the effect these uncertainties have on filter performance must be noted. A complete robustness analysis is beyond the scope of this thesis, but we provide here an overview and some preliminary results of such an analysis. Of particular importance are uncertainties arising in the following:

- mechanical properties, including the mass and stiffness,
- damping,
- electrostatic properties, including the forces generated by the comb drives,
- the input voltage signal, including any noise that may be present, and
- background system noise.

The importance of these uncertainties is largely due to the direct effect they have on filter characteristics, including,

- the linear natural frequency of the filter,
- the stability thresholds and the ability to manipulate them through linear tuning, and
- the system nonlinearities and the ability to manipulate them through nonlinear tuning.

8.1 Parameter Sensitivity

The robustness issues arising from design parameter uncertainty are perhaps best addressed through sensitivity analysis, as it offers a means through which the effects of parameter uncertainty can be estimated. For current purposes, the standard definition of sensitivity is used, namely,

$$S(A, B) = \frac{\partial A}{\partial B} \frac{B}{A}, \quad (8.1)$$

which represents in the percent change in A due to a percent change in B .

Due to the nature of the filtering method described within this work, the sensitivity of only two filter parameters are of utmost importance, namely, the sensitivity of ρ , which dictates the orientation of the instability region, and the sensitivity of ω_0 , which dictates the location of the apex of the instability region.

All other parameters, once designed within acceptable ranges, can deviate from their specified values with minimal loss of performance.

A brief analysis shows that calculating the sensitivity of ω_0 is trivial. In particular, one finds that

$$S(\omega_0, k_1) = \frac{1}{2}, \quad (8.2)$$

$$S(\omega_0, m) = -\frac{1}{2}. \quad (8.3)$$

As such, for every 1% change in m or k_1 , ω_0 will exhibit 0.5% change. As both the linear stiffness and the mass are highly predictable, this indicates that uncertainties associated with the purely elastic linear natural frequency will likely have minimal effect on the system.

The sensitivities associated the linear tuning parameter, ρ , however, are slightly more interesting. Recall from Equation 5.3 that

$$\rho = \frac{\nu_1}{\lambda_1} = 1 + \frac{r_{10}\alpha^2}{r_{1A}}, \quad (8.4)$$

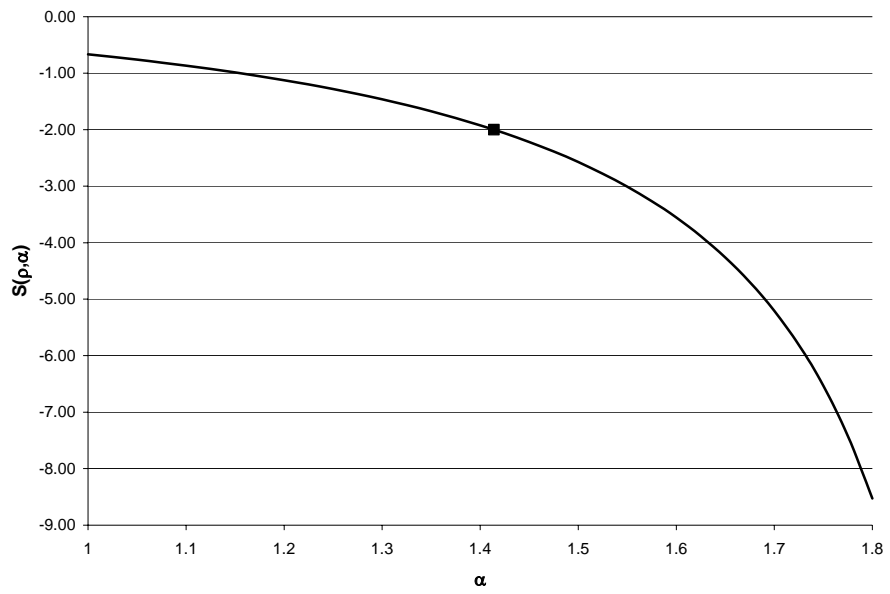
where r_{10} and r_{1A} are electrostatic coefficients dependent on the geometry of the fingers of the comb drives and α is a tuning parameter which specifies the relationship between AC and DC input voltages. Evaluating the sensitivities reveals that

$$S(\rho, \alpha) = \frac{2r_{10}\alpha}{r_{1A} + r_{10}\alpha^2}, \quad (8.5)$$

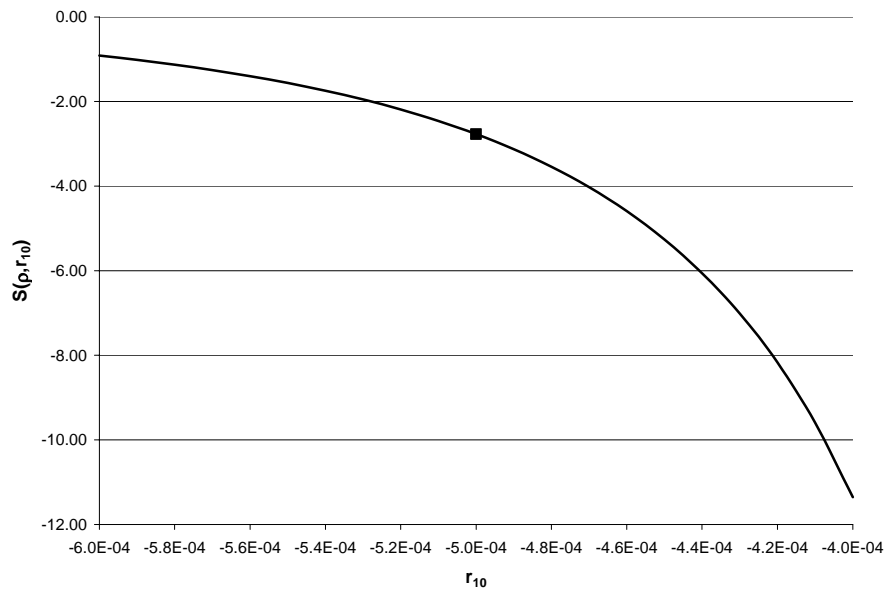
$$S(\rho, r_{10}) = \frac{r_{10}\alpha}{r_{1A} + r_{10}\alpha^2}, \text{ and} \quad (8.6)$$

$$S(\rho, r_{1A}) = -\frac{r_{10}\alpha}{r_{1A} + r_{10}\alpha^2}, \quad (8.7)$$

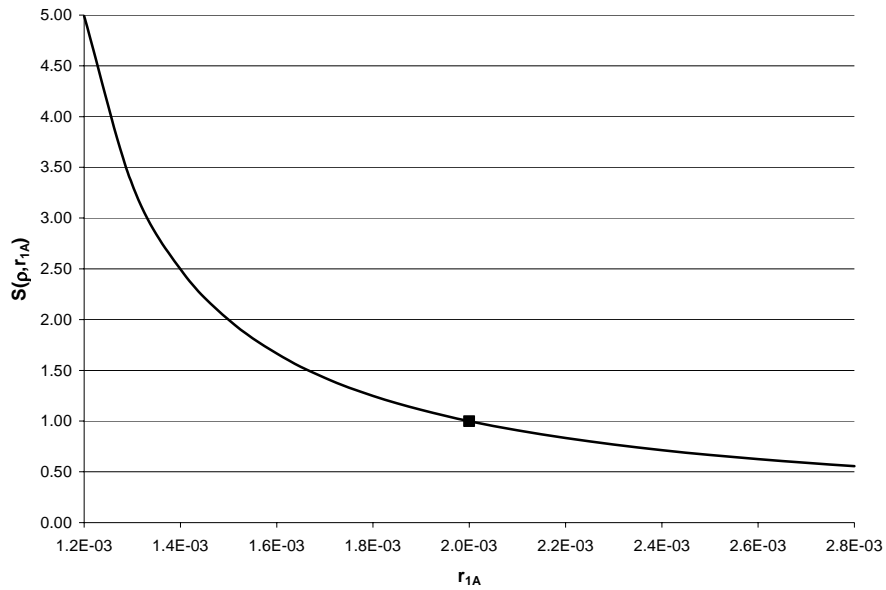
which, when plotted for the $\rho = 1/2$ oscillator design presented in Table 2 results in the sensitivity curves of Figure 16. From these plots it is clear that the linear electrostatic coefficients and the voltage tuning parameter must be selected with high precision to ensure the verticality of the stability boundary, and thus its amplitude independence. This is not difficult for the user-specified voltage ratio α . However, for r_{10} and r_{1A} this is easier said than done, as the electrostatic coefficients are determined largely through approximate methods, including electrostatic finite element techniques (typically a two-dimensional analysis) and curve fitting.



(a)



(b)



(c)

Figure 16. Sensitivity plots, which show the sensitivity of ρ with respect to each of its components. The black squares designate the nominal design parameters used for the $\rho = 1/2$ oscillator under consideration here.

8.2 Effects of Noise

While the sensitivity methods presented above are extremely useful for determining the required accuracy of system design parameters and the net effect parameter uncertainty will have on the system, another fundamental issue remains. In particular, the filter's capability to handle uncertain inputs must be considered. Whereas the analysis considered to this point has assumed perfectly harmonic input signals, in reality filters will also see both pure noise inputs and harmonic inputs with superimposed noise. While the effects such inputs have on this filter are beyond the scope of this work, it is worth noting that

a bevy of literature exists which examines the response of both single-degree-of-freedom (SDOF) and multi-degree-of-freedom (MDOF), parametrically-excited systems with stochastic inputs [56-65]. The complication here is that a full analysis of the system's response to stochastic inputs would require one to assume both random amplitude and phase, which would affect both the linear and nonlinear behavior of the oscillator, thus significantly complicating matters.

Chapter 9

Conclusions and Directions for Future Work

Filtering based on parametric excitation has some very attractive features, as summarized in Figure 15. For the implementation considered here, the most obvious drawbacks are:

- a damping-dependent critical AC excitation amplitude is required for operation (which can be addressed by restricting the input voltage to a specified range);
- design robustness issues may arise, for example, the required accuracies of the linear tuning strategy that rotates the wedge, temperature sensitivity, effects of noise, etc;
- the insertion loss of the physical system cannot yet be quantified, since this will depend on the hardware implemented for the filter;
- higher order resonances may appear in the system, which will lead to non-trivial responses well away from the passband; and
- one must be able to measure, or at least estimate, the amplitude of the harmonic input of interest.

These issues will be addressed in forthcoming studies, including planned experimentation.

In addition to the methods described within this work, a number of alternative filtering methods based on parametric excitation are currently under consideration. Amongst the most promising alternatives are:

- coupled oscillator filtering systems, designed such that logic circuitry, like that shown in Chapter 7, is unnecessary;
- parametrically-excited filters with specially tailored inputs, such as constant amplitude square waves, which may be used to avoid the amplitude dependent nature of a single oscillator's passband and center frequency; and
- parametrically-excited filters tailored to handle noise.

While this work focused on bandpass filters, it is worth noting that an equally ideal band gap filter can theoretically be produced by simply changing block P such that it enables with a zero amplitude signal instead of a non-zero amplitude signal. It is also expected that these parametric-based frequency switches can be used to develop high and low pass filters.

The ultimate goal of this line of work is to achieve fully functional filters wherein the parametrically excited MEM oscillators and the associated circuitry are integrated into a single chip.

REFERENCES

1. J. F. Rhoads, S. W. Shaw, K. L. Turner, and R. Baskaran. *Tunable MEMS Filters that Exploit Parametric Resonance*. (in preparation). 2004.
2. S. W. Shaw, K. L. Turner, J. F. Rhoads, and R. Baskaran. *Parametrically Excited MEMS-Based Filters*. IUTAM Symposium on Chaotic Dynamics and Control of Systems and Processes. 2003: (to be published).
3. K. Wang and C. T.-C. Nguyen. *High-Order Micromechanical Electronic Filters*. IEEE International Micro Electro Mechanical Workshop. 1997. Nagoya, Japan.
4. W. Zhang, R. Baskaran, and K. L. Turner. *Effect of Cubic Nonlinearity on Auto-Parametrically Amplified Resonant MEMS Mass Sensor*. Sensors and Actuators A: Physical. 2002. 102(1-2): p. 139-150.
5. S. G. Adams, F. Bertsch, and N. C. MacDonald. *Independent Tuning of Linear and Nonlinear Stiffness Coefficients*. Journal of Microelectromechanical Systems. 1998. 7(2): p. 172-180.
6. J. F. Rhoads, S. W. Shaw, B. E. Demartini, J. Moehlis, and K. L. Turner. *On the Response of Systems with Generalized Parametric Excitation Including Application to MEMS*. (in preparation). 2004.
7. J. P. Maxfield and H. C. Harrison. *Methods of High Quality Recording and Reproducing of Music and Speech Based on Telephone Research*. Bell System Technical Journal. 1926. 5: p. 493-523.
8. H. J. De Los Santos. *Introduction to Microwave Microelectromechanical Systems*. 1999, New York: Artech House.
9. G. A. Campbell. *Physical Theory of the Electric Wave-Filter*. Bell System Technical Journal. 1922. 1: p. 1-32.
10. R. A. Johnson, M. Borner, and M. Konno. *Mechanical Filters - A Review of Progress*. IEEE Transactions of Sonics and Ultrasonics. 1971. SU-18(3): p. 155-170.

11. R. Adler. *Compact Electromechanical Filters*. Electronics. 1947. 20: p. 100-105.
12. Y. Nakazawa. *High Frequency Crystal Electromechanical Filter*. Annual Frequency Control Symposium. 1962.
13. R. A. Sykes and W. D. Beaver. *High Frequency Monolithic Filters with Possible Application to Single Frequency and Single Side Band Use*. Annual Frequency Control Symposium. 1966.
14. J. T. Taylor and Q. Huang, eds. *CRC Handbook of Electrical Filters*. 1997, CRC Press: Boca Raton, Florida.
15. M. G. Ellis. *Electronic Filter Analysis and Synthesis*. 1994, New York: Artech House.
16. P. V. Wright. *A Review of SAW Resonator Filter Technology*. 1992 IEEE Ultrasonics Symposium. 1992.
17. F. Ishihara, Y. Koyamada, and S. Yoshikawa. *Narrow Band Filters Using Surface Acoustic Wave Resonators*. 1975 IEEE Ultrasonics Symposium. 1975.
18. J. Machui, J. Bauregger, G. Riha, and I. Schropp. *SAW Devices in Cellular and Cordless Phones*. 1995 IEEE Ultrasonics Symposium. 1995.
19. A. Antoniou. *Digital Filters: Analysis and Design*. 1979, New York: McGraw-Hill.
20. R. W. Hamming. *Digital Filters*. 1983, Englewood Cliffs: Prentice-Hall.
21. D. Schlichtharle. *Digital Filters: Basics and Design*. 2000, Berlin: Springer-Verlag.
22. F. Taylor. *Digital Filter Design Handbook*. 1984, New York: Marcel Dekker.

23. L. Lin, R. T. Howe, and A. P. Pisano. *Microelectromechanical Filters for Signal Processing*. Journal of Microelectromechanical Systems. 1998. 7(3): p. 286-294.
24. C. T.-C. Nguyen. *Micromechanical Filters for Miniaturized Low-Power Communications*. SPIE: Smart Structures and Materials (Smart Electronics and MEMS). 1999. Newport Beach, California.
25. C. T.-C. Nguyen. *Micromechanical Resonators for Oscillators and Filters*. 1995 IEEE International Ultrasonics Symposium. 1995. Seattle, Washington.
26. B. Piekarski, D. DeVoe, M. Dubey, R. Kaul, J. Conrad, and R. Zeto. *Surface Micromachined Piezoelectric Resonant Beam Filters*. Sensors and Actuators A: Physical. 2001. 91(3): p. 313-320.
27. V. K. Varadan, K. J. Vinoy, and K. A. Jose. *RF MEMS and Their Applications*. 2003, West Sussex: John Wiley & Sons.
28. Raytheon. *Raytheon Demonstrates 25-watt RF Filter Using MEMS Technology*. www.raytheon.com/press/2000/jan/mems.html.
29. C. T.-C. Nguyen. *Micromechanical Circuits for Wireless Communications*. 2000 European Solid-State Device Research Conference. 2000. Cork, Ireland.
30. C. T.-C. Nguyen. *Microelectromechanical Devices for Wireless Communications*. 1998 IEEE International Micro Electro Mechanical Systems Workshop. 1998. Heidelberg, Germany.
31. K. Wang and C. T.-C. Nguyen. *High-Order Medium Frequency Micromechanical Electronic Filters*. Journal of Microelectromechanical Systems. 1999. 8(4): p. 534-557.
32. C. T.-C. Nguyen. *High-Q Microelectromechanical Oscillators and Filters for Communications*. 1997 IEEE International Symposium on Circuits and Systems. 1997. Hong Kong.

33. C. T.-C. Nguyen. *Vibrating RF MEMS for Low Power Communications*. 2000 International MEMS Workshop (iMEMS '01). 2000. Singapore.
34. A. B. Williams. *Electronic Filter Design Handbook*. 1981, New York: McGraw-Hill.
35. A. H. Nayfeh and D. T. Mook. *Nonlinear Oscillations*. 1979: Wiley-Interscience.
36. M. Faraday. *On a Peculiar Class of Acoustical Figures and on Certain Forms Assumed by a Group of Particles Upon Vibrating Elastic Surfaces*. Philosophical Transactions of the Royal Society. 1831. 121: p. 299-340.
37. J. J. Stoker. *Nonlinear Vibrations in Mechanical and Electrical Systems*. 1950, New York: John Wiley & Sons.
38. B. van der Pol and M. J. O. Strutt. *On the Stability of the Solutions of Mathieu's Equation*. The London, Edinburgh, and Dublin Philosophical Magazine and Journal of Science (Seventh Series). 1928. 5: p. 18-38.
39. P. Srinivasan. *Nonlinear Mechanical Vibrations*. 1995, New Delhi: New Age International Limited.
40. E. L. Ince. *Ordinary Differential Equations*. 1956: Dover Publications.
41. J. K. Hale. *Oscillations in Nonlinear Systems*. Advanced Mathematics with Applications, ed. S. Lefschetz and J.P. LaSalle. 1963, New York: MacGraw-Hill.
42. D. W. Jordan and P. Smith. *Nonlinear Ordinary Differential Equations*. 2nd ed. Oxford Applied Mathematics and Computing Science Series, ed. J.N. Buxton, R.F. Churchhouse, and A.B. Tayler. 1987, Oxford: Oxford University Press.
43. R. Campbell. *Theorie Generale De L'Equation De Mathieu*. 1955, Paris: Masson et Cie.

44. S. V. Simakhina. *Stability Analysis of Hill's Equation, Department of Mathematics, Statistics, and Computer Science*. 2003, University of Illinois at Chicago: Chicago.
45. K. L. Turner, S. A. Miller, P. G. Hartwell, N. C. MacDonald, S. H. Strogatz, and S. G. Adams. *Five Parametric Resonances in a Microelectromechanical System*. *Nature*. 1998. 396: p. 149-152.
46. K. L. Turner. *Applications and Analysis of Parametric Resonance in Microelectromechanical Systems*. 1999, Cornell University: Ithaca.
47. K. L. Turner and N. C. MacDonald. *Understanding Parametric Resonance Effects in Common MEM Actuators*. Hilton Head 2000, Solid-State Sensors and Actuators Workshop. 2000. Hilton Head, South Carolina.
48. K. L. Turner, P. G. Hartwell, F. M. Bertsch, and N. C. MacDonald. *Parametric Resonance in a Microelectromechanical Torsional Oscillator*. 1998 ASME International Mechanical Engineering Congress and Exposition, Micro-Electro-Mechanical Systems. 1998.
49. W. Zhang and K. Turner. *Parametrically Resonant Mass Sensor*. Workshop on Solid-State Sensors and Actuators. 2004. Hilton Head, South Carolina: to be published.
50. W. C. Tang, T.-C. H. Nguyen, M. W. Judy, and R. T. Howe. *Electrostatic-comb Drive of Lateral Polysilicon Resonators*. *Transducers '89, the 5th International Conference on Solid-State Sensors and Actuators and Eurosensors III*. 1990.
51. W. C. Tang, T.-C. H. Nguyen, and R. T. Howe. *Laterally Driven Polysilicon Resonant Microstructures*. *Sensors and Actuators*. 1989. 20: p. 25-32.
52. W. Zhang, R. Baskaran, and K. L. Turner. *Tuning the Dynamic Behavior of Parametric Resonance in a Micromechanical Oscillator*. *Applied Physics Letters*. 2003. 82(1): p. 130-132.
53. S. H. Strogatz. *Nonlinear Dynamics and Chaos with Applications to Physics, Biology, Chemistry, and Engineering*. 1994, Cambridge: Westview.

54. B. E. Demartini. *Unpublished Notes*. 2004.
55. *Simulink*. 2001, Mathworks.
56. N. S. Namachchivaya and N. Ramakrishnan. *Stochastic Dynamics of Parametrically Excited Two D.O.F. Systems with Symmetry*. Journal of Sound and Vibration. 2003. 262(3): p. 613-631.
57. R. A. Ibrahim. *Parametric Random Vibration*. 1985, Letchworth: Research Studies Press.
58. R. A. Ibrahim and A. Pandya. *Functional-Perturbational Analysis of Non-Linear Systems Under Random External and Parametric Excitations*. Journal of Sound and Vibration. 1990. 137(3): p. 443-455.
59. H. Rong, W. Xu, and T. Fang. *Principal Response of Duffing Oscillator to Combined Deterministic and Narrow-Band Random Parametric Excitation*. Journal of Sound and Vibration. 1998. 210(4): p. 483-515.
60. H. Rong, G. Meng, X. Wang, W. Xu, and T. Fang. *Invariant Measures and Lyapunov Exponents for Stochastic Mathieu System*. Nonlinear Dynamics. 2002. 30(4): p. 313-321.
61. V. Kagalovsky, J. Haddad, and S. Tapuchi. *Weak Non-Linearity Effect on Stochastic Parametric Resonance*. Journal of Sound and Vibration. 2001. 239(3): p. 565-568.
62. M. F. Dimentberg, Z. Hou, and M. Noori. *Stability of an SDOF System Under Periodic Parametric Excitation with a White Noise Phase Modulation*, in *Nonlinear Dynamics and Stochastic Mechanics*, W.H. Kliemann and N.S. Namachchivaya, Editors. 1995, CRC Press. p. 341-359.
63. M. Dimentberg, Z. Hou, M. Noori, and W. Zhang. *Response of an SDOF System to Periodic External and Parametric Excitations with Random Phase Modulations*. Journal of Sound and Vibration. 1996. 192(3): p. 621-627.

64. J. J. Brouwers. *Stability of a Non-Linearly Damped Second-Order System with Randomly Fluctuating Restoring Coefficient*. International Journal of Nonlinear Mechanics. 1986. 21(1): p. 1-13.

65. W. Wedig. *Parametric Instability and Process Identification*, in *Analysis and Estimation of Stochastic Mechanical Systems*, W. Schiehlen and W. Wedig, Editors. 1988, Springer-Verlag: Wien.